nature structural & molecular biology

ARTICLES

https://doi.org/10.1038/s41594-022-00779-7

Check for updates

Structure, dynamics and assembly of the ankyrin complex on human red blood cell membrane

Xian Xia[1,2,3], Shiheng Liu[1,2,3] and Z. Hong Zhou[1,2] ✉

The cytoskeleton of a red blood cell (RBC) is anchored to the cell membrane by the ankyrin complex. This complex is assembled during RBC genesis and comprises primarily band 3, protein 4.2 and ankyrin, whose mutations contribute to numerous human inherited diseases. High-resolution structures of the ankyrin complex have been long sought-after to understand its assembly and disease-causing mutations. Here, we analyzed native complexes on the human RBC membrane by stepwise fractionation. Cryo-electron microscopy structures of nine band-3-associated complexes reveal that protein 4.2 stabilizes the cytoplasmic domain of band 3 dimer. In turn, the superhelix-shaped ankyrin binds to this protein 4.2 via ankyrin repeats (ARs) 6–13 and to another band 3 dimer via ARs 17–20, bridging two band 3 dimers in the ankyrin complex. Integration of these structures with both prior data and our biochemical data supports a model of ankyrin complex assembly during erythropoiesis and identifies interactions essential for the mechanical stability of RBC.

The human red blood cell (RBC, or the erythrocyte) is the most abundant cell in our blood and the principal gas exchanger between O_2 and CO_2 in our bodies. Devoid of a nucleus, the RBC has been engineered for a wide range of medical applications[1]. RBC exhibits an unusual biconcave disc shape and remarkable membrane mechanical stability, both of which are essential for cycling through the vasculature for O_2–CO_2 exchange. These properties are endowed by the RBC cytoskeleton, which is bridged to the RBC membrane by the junctional complex and ankyrin complex[2]. The ankyrin complex, which primarily contains band 3, protein 4.2, ankyrin and Rh subcomplex, connects the cytoskeleton to the membrane through the cytoplasmic domain of band 3 (refs. [3,4]). Defects in these cytoskeleton and cytoskeleton-associated proteins are associated with numerous human hereditary diseases, such as hereditary spherocytosis, South Asian ovalocytosis and hereditary stomatocytosis[5,6].

Mass spectrometry and biochemical analyses of complexes from detergent-treated RBC membranes have shown that band 3, protein 4.2 and ankyrin interact with one another[7,8], and that ankyrin repeats (ARs) 13–24 of ankyrin bind to the cytoplasmic domain of band 3 (refs. [9–11]). Protein 4.2 is a peripheral membrane protein with amino-terminal myristoylation[12] and shares homology with transglutaminases but lacks transglutaminase activity[13,14]. Crystal structures are available separately for the membrane domain and cytoplasmic domain of band 3 (refs. [15,16]), as well as ARs 13–24 of ankyrin[17]. However, there are no structures available for any full-length proteins, let alone for any complexes containing them. Consequently, our understanding regarding the molecular interactions underlying the assembly and disease-causing mutations of the ankyrin complex remains extremely limited. In this study, we obtained native band 3, band 3–protein 4.2 complex and ankyrin complex centered on band 3, protein 4.2 and ankyrin (Fig. 1a) by stepwise fractionation of the erythrocyte membrane. A total of nine near-atomic resolution structures with various subunits of band 3, protein 4.2 and ankyrin were determined by cryo-EM, unraveling details of their interactions for the first time. These structures, combined with both prior and our biochemical data and knowledge about disease-causing mutations, support a model of ankyrin complex assembly during erythropoiesis and reveal the importance of these interactions in linking the cytoskeleton to the membrane in RBCs.

Results

Isolation of native band-3-associated complexes. To obtain the structures of full-length band 3 and related protein complexes, we analyzed the native proteins from human erythrocyte membrane by stepwise fractionation (Extended Data Fig. 1). Detergent solubilization of the erythrocyte membrane gave rise to three fractions: low-salt fraction, high-salt fraction 1 and high-salt fraction 2. To stabilize the ankyrin complex in the high-salt fraction 2 for cryo-EM, GraFix (Gradient Fixation)[18] with glutaraldehyde was applied.

SDS-PAGE and cryo-EM analyses both show that the predominant species in the low-salt fraction is band 3 (Extended Data Figs. 1b and 2c). The native band 3 is a dimer (Fig. 1b and Extended Data Fig. 2), and at an overall resolution of 4.8 Å, its structure reveals both the membrane domain (mdb3) and cytoplasmic domain (cdb3), each of which is similar to the crystal structures of mdb3 (ref. [16]) and cdb3 (ref. [15]), respectively. Though not resolved to high resolution, the cryo-EM density accommodates a cdb3 dimer structure with the characteristic reverse V-shape groove[19], indicating that the structure of the band 3 dimer resolved here is in the reversed-V (rev-V) conformation (Extended Data Fig. 2g).

From the high-salt fraction 1, we identified 4 complexes—each containing a band 3 dimer (B_2) and a differently associated or oriented (either loosely associated, or tightly associated in vertical (75°) or diagonal (45°) orientation to the membrane) protein 4.2 as either a monomer (P_1) or dimer (P_2)—designated as $B_2P_1^{loose}$ (overall resolution 4.1 Å), $B_2P_1^{vertical}$ (4.6 Å), $B_2P_2^{vertical}$ (4.6 Å) and $B_2P_1^{diagonal}$ (3.6 Å) (Table 1, Extended Data Fig. 3 and Supplementary Video 1). All of them have identical interaction between the cdb3 and protein 4.2. The majority (56%) of the complexes were the $B_2P_1^{diagonal}$ complex (Fig. 1c and Extended Data Fig. 3c). Focused refinement further improved the resolution of the membrane (mdb3) and the cytoplasmic (cdb3 and protein 4.2) region to 3.3 Å and 3.1 Å, respectively (Extended Data Fig. 3c). Although loosely associated to band 3 on the basis of its less robust density, protein 4.2 in $B_2P_1^{loose}$

[1]Department of Microbiology, Immunology, and Molecular Genetics, University of California, Los Angeles, CA, USA. [2]California NanoSystems Institute, University of California, Los Angeles, CA, USA. [3]These authors contributed equally: Xian Xia, Shiheng Liu. ✉e-mail: Hong.Zhou@UCLA.edu

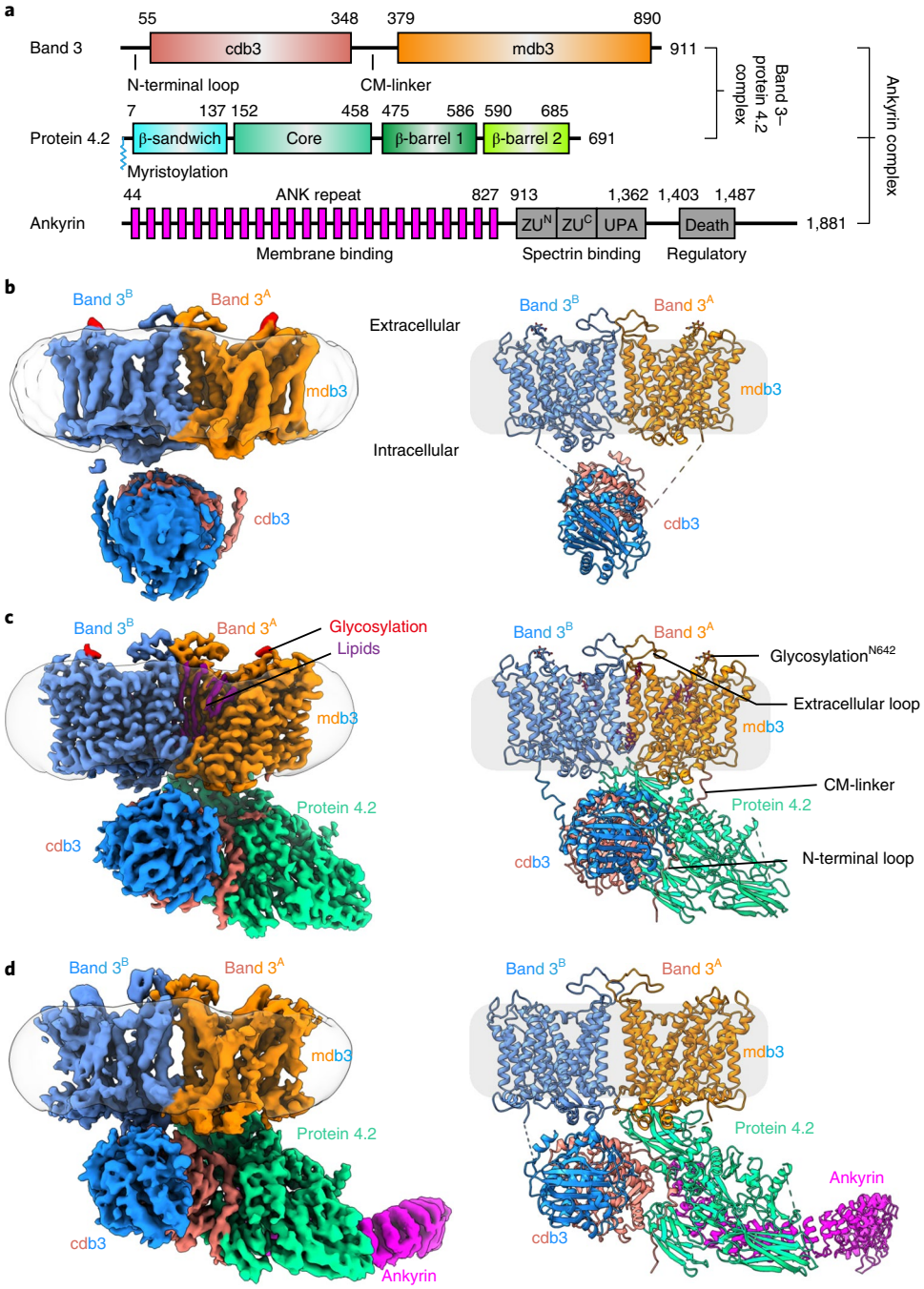

Fig. 1 | Cryo-EM structures of band 3, protein 4.2 complex and ankyrin-containing complex. a, Schematic illustrating domain organizations of band 3, protein 4.2 and ankyrin. Residue numbers at domain boundaries are indicated. CM-linker in band 3 represents the linker between cdb3 and mdb3. The myristoylation site of protein 4.2 at the N-terminal residue Gly2 is indicated. **b**–**d**, Cryo-EM maps and atomic models of the band 3 dimer (**b**), $B_2P_1^{diagonal}$ complex (**c**) and $B_2P_1A_1$ complex (**d**). The detergent belts are shown in transparent gray, depicting membrane boundaries. The maps in **c** and **d** are generated from focus-refined maps combining membrane and cytoplasmic parts.

is oriented the same as it is in $B_2P_1^{vertical}$. In the structure of $B_2P_2^{vertical}$, the two protein 4.2 subunits do not interact with each other; rather, each subunit independently binds to a cdb3 of the band 3 dimer with twofold symmetry.

Two ankyrin-bound complexes were obtained from the high-salt fraction 2, both containing $B_2P_1^{diagonal}$ but with either one or two ankyrin molecules, which we designate as $B_2P_1A_1$ (4.4 Å) or $B_2P_1A_2$ (5.7 Å), respectively (Fig. 1d, Table 1 and Extended Data Fig. 4). Reprocessing the same particles extracted with a larger box size enabled visualization of ankyrin assembled on two dimers of band 3 (B_4), which we designate as $B_4P_1A_1$ and $(B_2P_1A_1)_2$ (Extended Data Fig. 4c).

In total, we isolated nine native band-3-associated complexes. Interactions among subunits of the band-3-associated complexes and related mutations, including those that cause human diseases, are detailed below.

Structure of the full-length band 3. Previous efforts to obtain a full-length band 3 structure have not been fruitful. We found that, in the absence of protein 4.2, native full-length band 3 existed as

Table 1 | Cryo-EM data collection, refinement and validation statistics

EMDB (focused refinement)	Band 3 (EMD-26148)	$B_2P_1^I$ (EMD-26145)	$B_2P_1^v$ (EMD-26146)	$B_2P_2^v$ (EMD-26147)	$B_2P_1^d$ (EMD-26142, EMD-26143, EMD-26144)	$B_2P_1A_1$ (EMD-26149, EMD-26150)	$B_2P_1A_2$ (EMD-26151, EMD-26152)	$B_4P_1A_1$ (EMD-26153)	$(B_2P_1A_1)_2$ (EMD-26154)
PDB	7TW2		7TW0	7TW1	7TVZ	7TW3	7TW5	7TW6	
Data collection and processing									
Magnification	105,000×	81,000×	81,000×	81,000×	81,000×	81,000×	81,000×	81,000×	81,000×
Camera	K2	K3	K3	K3	K3	K3	K3	K3	K3
Voltage (kV)	300	300	300	300	300	300	300	300	300
Electron exposure ($e^-/Å^2$)	50	50	50	50	50	50	50	50	50
Defocus range (μm)	−1.8 to −2.6	−1.8 to −2.6	−1.8 to −2.6	−1.8 to −2.6	−1.8 to −2.6	−1.8 to −2.6	−1.8 to −2.6	−1.8 to −2.6	−1.8 to −2.6
Pixel size (Å)	1.062	1.1	1.1	1.1	1.1	1.1	1.1	2.2	2.2
Symmetry imposed	C_1	C_1	C_1	C_2	C_1	C_1	C_1	C_1	C_1
Particle number	530,000	446,000	104,000	104,000	962,000	384,000	63,000	322,000	53,000
Map resolution	4.8	4.1	4.6	4.6	3.6 (3.3/3.1)	4.4 (4.1)	5.7 (4.4)	5.6	8.5
FSC threshold	0.143	0.143	0.143	0.143	0.143	0.143	0.143	0.143	0.143
Refinement									
Map sharpening *B* factor ($Å^2$)	−237		−192	−212	−190	−214	−324	−326	
Model resolution (Å)	4.1		3.9	3.8	3.5	4.4	5.6	5.5	
FSC threshold	0.143		0.143	0.143	0.143	0.143	0.143	0.143	
Model composition									
Non-hydrogen atoms	12,838		18,266	23,625	18,659	22,641	27,048	27,184	
Protein residues	1,619		2,309	2,993	2,340	2,944	3,579	3,515	
Ligand	2		2		9				
B factors ($Å^2$)									
Protein	457.5		196.0	191.9	68.9	276.3	258.2	592.2	
Ligand	306.2		196.9		74.0				
R.m.s. deviations									
Bond lengths (Å)	0.003		0.003	0.003	0.002	0.004	0.003	0.004	
Bond angles (°)	0.754		0.729	0.744	0.500	0.748	0.769	0.759	
Validation									
MolProbity score	1.56		1.33	1.47	1.34	1.68	1.84	1.68	
Clashscore	9.46		5.6	7.46	4.08	9.8	12.0	10.2	
Poor rotamers (%)	0.07		0	0	0	0.08	0	0.03	
Ramachandran plot									
Favored (%)	97.8		97.9	97.7	97.2	97.0	96.7	97.2	
Allowed (%)	2.2		2.1	2.3	2.8	3.0	3.3	2.8	
Disallowed (%)	0		0	0	0	0	0	0	

a dimer in the low-salt fraction, and only the membrane domains were well resolved (Fig. 1b). This low-resolution nature of cdb3 is consistent with the previous observations that the CM-linker that bridges the cytoplasmic and the anchored membrane domains is flexible[19–21]. Among the nine band-3-associated complexes mentioned above, $B_2P_1^{diagonal}$ has the highest resolution,with both mdb3 and cdb3 domains resolved, as well as their linker, suggesting that binding of protein 4.2 restricts the relative movement of mdb3 and cdb3. Because $B_2P_1^{diagonal}$ has the best resolution, subsequent description of the band 3 structure will be based on this complex, unless otherwise stated.

This first atomic structure of the native, full-length band 3 reveals long sought-after structural features. Compared with the domain crystal structures of mdb3 (ref. [16]) and cdb3 (ref. [15]), our native band 3 structure (Fig. 1c and Extended Data Figs. 5a and 6) is not only full-length, but also contains previously unresolved regions: N-terminal loop (aa 30–55), CM-linker (aa 350–369), residues 641–648 with the N-glycan site N642, a long external loop (aa 554–566) and the mdb3-bound lipids. The dimer interface of mdb3 is similar to that in the crystal structure. But in the dimer interface of the cryo-EM maps, we resolved densities of several lipids or detergent molecules, which may facilitate the dimerization of band 3. There are no obvious interactions between the cdb3 and mdb3. Band 3 is a Cl^-–HCO_3^- exchanger and belongs to the SLC4 family[22]. In all our cryo-EM structures, mdb3 adopts an outward-facing conformation, as that of the mdb3 crystal structure locked by the inhibitor H_2DIDS[16] with a root mean square deviation (RMSD) of 0.931 Å for 443 of its 475 Cα atoms (Extended Data Fig. 5a,b). The N-terminal

ends of the two transmembrane helices (TM3 and TM10) face each other and create a positive dipole, which may provide the binding site for substrate anions (Extended Data Fig. 5d,e). Remarkably, near residues R730 and E681 in the helical dipole, densities for four putative water molecules were observed, three of which possibly delineate the substrate-binding site, as was also predicted from the structure of substrate-bound SLC4 (NDCBE[23]), SLC23 (UraA[24]) and SLC26 (BicA[25]) family transporters (Extended Data Fig. 5d,e). Consistent with this assignment, mutation of the residue R748 or E699 in murine band 3 (equivalent to R730 and E681 in human band 3, respectively) resulted in loss of Cl^-–HCO_3^- exchange[26–28], highlighting the importance of these residues in anion transport activity. Intriguingly, one molecule of *N*-dodecyl–β-D-maltoside (DDM) was identified at the interface between the gate and core domain of mdb3 (Extended Data Fig. 5c). Unlike H_2DIDS, the DDM molecule does not block the substrate-binding site. Instead, it may lock the relative rocking movement between the gate and core that is responsible for Cl^-–HCO_3^- translocation, leading to the observed outward-facing conformation.

Protein 4.2 and its interactions with band 3. Efforts to determine the structure of protein 4.2 have hitherto been hindered by difficulties in obtaining purified protein 4.2 in soluble form. The atomic model of protein 4.2 built from our cryo-EM structure of the $B_2P_1^{diagonal}$ complex contains 663 of its 691 residues. It has a triangular shape, with the body of the triangle formed by the core domain and the three vertices each formed by a domain with an immunoglobulin (Ig)-like fold[29] (Fig. 2a and Extended Data Fig. 7a–e). These domains are sequential in sequence, and their folds and architecture are both similar to those of the transglutaminase family of enzymes in the closed conformation[13,30–32] (RMSD of 3.898 Å with PDB 1L9N across 651 Cα atom pairs) (Fig. 2b). Therefore, we will use the transglutaminase domain names to describe corresponding domains of protein 4.2, that is, β-sandwich (aa 7–137, h-type Ig-like fold), core (aa 152–457), first (aa 475–586) and second (aa 590–685) β-barrel domains (s-type Ig-like fold), from the N to C terminus.

The core domain has a globular shape with ten helices (α3–α12) flanking the ten β strands (β10–β19) that form three β-sheets in the middle (Extended Data Fig. 7a). Notably, the catalytic triads, C272, H330 and D353, in transglutaminase are replaced by A268, Q327 and H350, respectively (Extended Data Figs. 7b and 8); the three corresponding residues are more separated from each other in protein 4.2 than in transglutaminase (Extended Data Fig. 7b). The biochemically identified ATP-binding loop (P-loop, aa 316–322)[33] in this domain is situated at its interface with β-barrel 1 (Fig. 2d), with a shift of ~5 Å towards β-barrel 1 compared with the corresponding loop of transglutaminase (PDB: 1L9N)[31]. Intriguingly, a Ca^{2+}-binding site in transglutaminase (PDB: 1L9N)[31] corresponds to the N terminus of helix α12 and the loop around β17 in the protein 4.2 core structure, both of which are closer to the β-barrel 1 domain than in transglutaminase (Fig. 2d). Although no ATP or calcium were observed in our structure, these shifts suggest that ATP binding/hydrolysis or calcium binding may induce conformational changes to protein 4.2 (ref. [30]), and these possibly modulate interactions with ankyrin (see below).

The three Ig-like domains share typical β-strand topology, but the N-terminal proximal one (β-sandwich) contains one additional strand (d) and two short helices (Extended Data Fig. 7c–e). Upon binding of cdb3, β-barrel 2 and the region near α7 (aa 227–268) shift towards band 3 (Fig. 2c). The membrane-proximal region of protein 4.2 is connected to the density of detergent micelles and contains predominantly positively charged residues (Extended Data Fig. 7f). These structural observations are consistent with previous observations that protein 4.2 is myristoylated at the N-terminal glycine residue and anchored to the lipid bilayer[12,34].

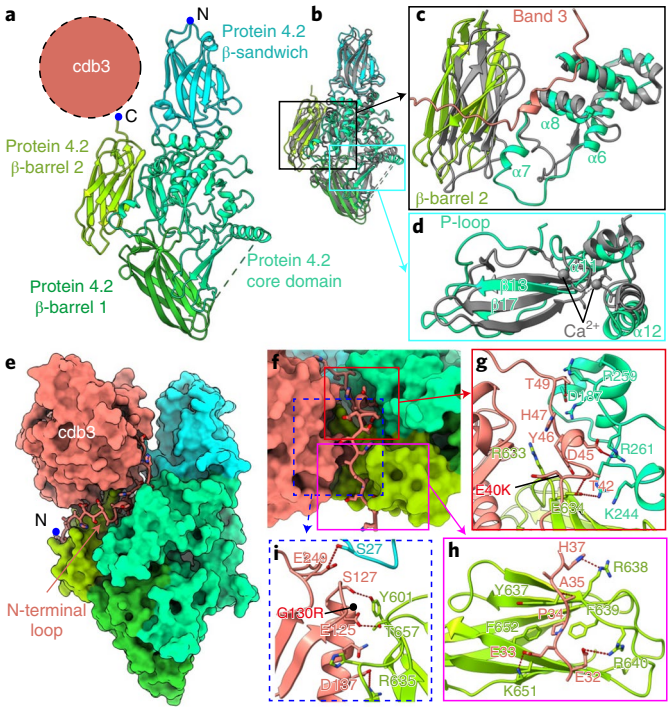

Fig. 2 | Protein 4.2 and its interactions with band 3. a, Structure of protein 4.2, shown in ribbons. The position of cdb3 is indicated by the dashed circle. **b**, Superposition of protein 4.2 with transglutaminase (gray, PDB: 1L9N) to identify structural differences in protein 4.2. **c**, Movements of β-barrel 2 and α7 of core domain in protein 4.2. **d**, Shifts of the P-loop and α12 in protein 4.2. **e**, Interactions of the N-terminal loop of band 3 with protein 4.2. Protein 4.2 and cdb3 are shown as surface, the N-terminal loop of band 3 is shown as in ribbon mode and side chains are shown as sticks. **f**, Enlarged view of the N-terminal loop in **e**. Three important regions are boxed: region 1 (red box) indicates the interactions around residues 40 to 50 of the N-terminal loop; region 2 (magenta box) indicates the interactions around residues 30 to 40 of N-terminal loop; region 3 (dashed blue box) shows the interactions between cdb3 and protein 4.2. **g–i**, Details of the interactions in boxed regions of **f**. Residues involved in the interactions are shown as sticks. Red dashed lines indicate hydrogen bonds and electrostatic interactions. Disease mutations (E40K and G130R) on band 3 are indicated by black dots.

Among the eight protein-4.2-containing structures, the interactions between band 3 and protein 4.2 are nearly identical. On band 3, this interaction is essentially through its cytoplasmic domain. The N-terminal loop (aa 30–55) was disordered in the absence of protein 4.2 and became ordered and visible upon binding protein 4.2 (Fig. 2e). The binding interface between band 3 and protein 4.2 can be divided into three regions (Fig. 2f). In region 1, a short helix and nearby loops of band 3 are docked into the groove formed by the core and the β-sandwich domains of protein 4.2 (Fig. 2g). The interactions include hydrogen bonds (band 3–protein 4.2: T42–E634, T49–D187) and electrostatic interaction between band 3 D45 and protein 4.2 R261, as well as hydrophobic interaction requiring band 3 Y46. In region 2, the band 3 loop (aa 30–39) lies on the surface of β-barrel 2 of protein 4.2. This interaction is mostly mediated by electrostatic interactions and hydrogen bonds (band 3–protein 4.2: E32–R640, E33–K651, A35–R638, H37–S636), while the hydrophobic interaction involving P34 of band 3 also strengthens the interaction (Fig. 2h). In region 3, residues around α3 (aa 120–150) and the loop after β7 (aa 249–250) in cdb3 form hydrogen bonds with protein 4.2's β-barrel 2 domain and the β-sandwich domain, respectively (Fig. 2i). Besides the major interface described above, the

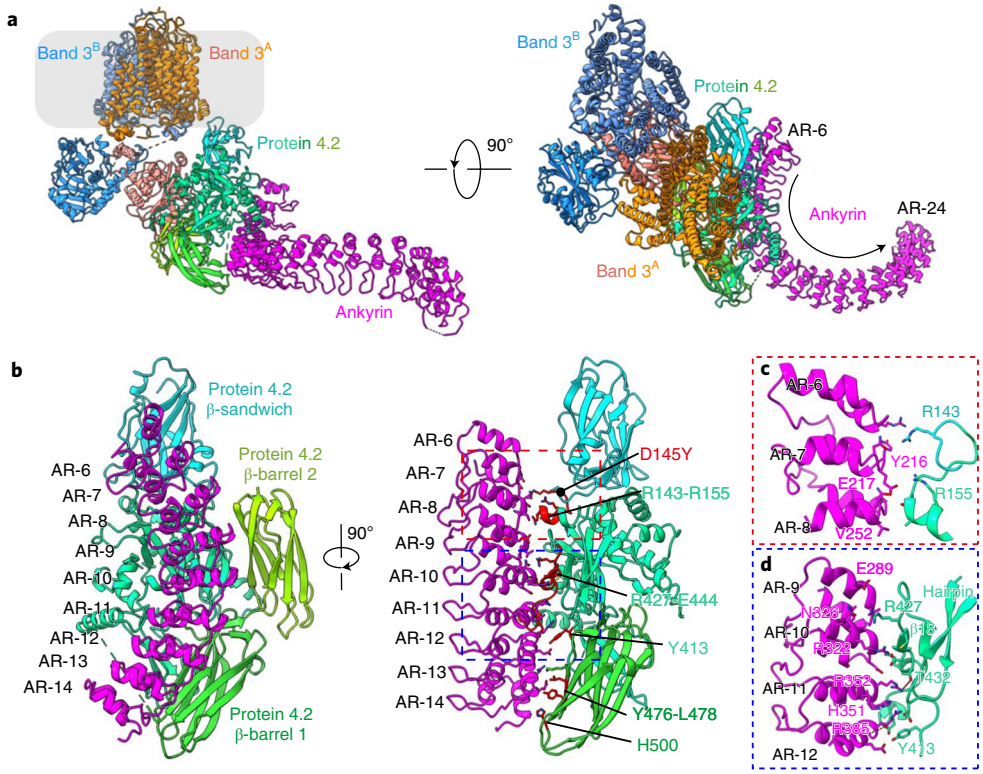

Fig. 3 | Anchorage of ankyrin to protein 4.2. a, Atomic model of the $B_2P_1A_1$ complex shown as ribbons. Approximate boundaries of the membrane are indicated in transparent gray. **b**, Different views of the protein 4.2–ankyrin interface. Band 3 and ARs 15–24 of ankyrin are omitted for clarity. Residues of protein 4.2 that are involved in ankyrin interaction are colored in red and labeled. A disease mutation (D145Y) on protein 4.2 is indicated by a black dot. **c**,**d**, Details of interactions in boxed regions of **b**.

CM-linker of band 3 interacts with the core domain of protein 4.2, further stabilizing the $B_2P_1^{diagonal}$ complex (Extended Data Fig. 9f–h), which is not observed in the $B_2P_1^{vertical}$ and $B_2P_2^{vertical}$ complexes. Notably, protein 4.2 does not interact with mdb3 specifically; rather, the mdb3 proximal N terminus of protein 4.2 can restrict the rocking movement between the gate and core domains of mdb3 needed for ion exchange/transport. Such restriction might be the reason why band 3's capability for ion transport decreases after binding with protein 4.2 (ref. [35]). These close interactions between band 3 and protein 4.2 are consistent with both biochemical observations and disease-causing mutations. Protein 4.2 can be purified from the membrane only by relatively harsh treatments[36,37]. Two hereditary spherocytosis mutations (E40K and G130R)[38,39] in cdb3, which lead to disproportionate loss of protein 4.2, are located on these binding interfaces (Fig. 2g,i), further highlighting the essential role of band 3-protein 4.2 interaction in the function of erythrocytes.

Anchorage of ankyrin to protein 4.2 and band 3. Previous crystal structures of recombinantly expressed ankyrin fragments indicated that the 89-kDa N-terminal membrane binding domain of erythrocyte ankyrin consists of 24 ankyrin repeats of approximately 33 amino acids each[17,40]. ARs 6–24 were modeled in our cryo-EM density maps of the four ankyrin-containing complexes ($B_2P_1A_1$, $B_2P_1A_2$, $B_4P_1A_1$ and $(B_2P_1A_1)_2$) (Fig. 3a and Extended Data Fig. 10a,b,e). No global structural changes occur in either band 3 or protein 4.2 in these complexes upon ankyrin binding.

The interactions between ankyrin and protein 4.2 are the same in all four ankyrin-containing complexes; therefore, we focused our description below on $B_2P_1A_1$, which has the best resolution (4.1 Å) for the region involving ankyrin-protein 4.2 interactions. Protein 4.2 interacts extensively with ARs 6–13 of ankyrin via a conserved surface on its core and β-barrel 1 domains (Fig. 3b and Extended Data Figs. 7h and 8). Overall, these two domains clamp ankyrin, with major binding sites located in the core domain of protein 4.2. Specifically, residues around α3 (aa R143–E152) of protein 4.2 interact with ARs 6–8 of ankyrin via hydrogen bonds, whereas residues between β17 and α12 (aa Y413–E439) contact extensively with ARs 9–12 through both hydrogen bonds and hydrophobic interactions (hydrophobic stacking between Y413 of protein 4.2 and R385 and H351 of ankyrin) (Fig. 3c,d and Extended Data Fig. 8). This ankyrin–protein 4.2 binding is further strengthened by contacts between the β-barrel 1 of protein 4.2 (residues Y476–L478 and H500) and AR-13 of ankyrin (Fig. 3b). The previously identified hairpin of protein 4.2 (N163–D180) in the core domain[13,41] has no interaction with band 3, but instead is close to AR-11 of ankyrin and thus may facilitate the association between protein 4.2 and ankyrin (Fig. 3d).

Besides interacting with protein 4.2, ankyrin also directly contacts band 3 in three ($B_2P_1A_2$, $B_4P_1A_1$ and $(B_2P_1A_1)_2$) of the four ankyrin-containing complexes (Fig. 4a and Extended Data Fig. 10a,b,e), specifically with ARs 17–20 binding cdb3. The details of this binding are illustrated with $B_2P_1A_2$ (4.6 Å after focused classification) (Fig. 4b), including the following three sets of amino acids between ankyrin and band 3: AR-17 (L556–Q563) and AR-18 (aa R590–H596) with band 3 residues near α3 (aa S127–G130) and β7 (aa E252–E257), AR-19 (aa R619–S627) with band 3 residues E151–K160 near α4, and AR-20 (aa K657–L663) with band 3's loop residues K69–E72 and D183.

Biochemical data further confirmed these observed interactions between band 3 and ankyrin. First, our pull-down assay showed that the mutations G130R (disease mutation) on band 3 α3 and R155A on band 3 α4 eliminated ankyrin binding. In addition, ankyrin truncations ARs 18–24, ARs 19–24 and ARs 20–24, as well as mutations on AR-19 (Q623A and Y624A), abolished band 3 interaction (Fig. 4c), further validating the atomic details of the band 3-ankyrin

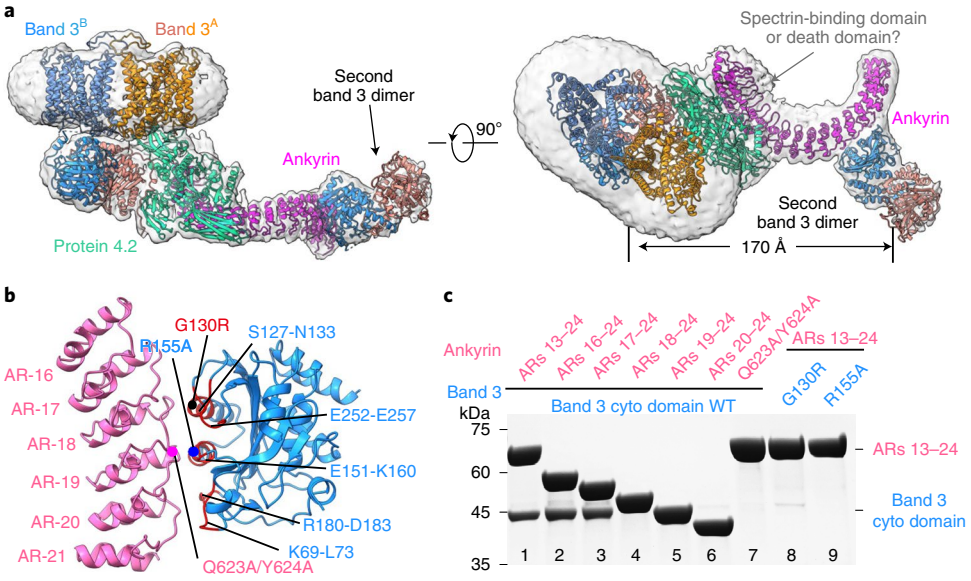

Fig. 4 | Interaction of ankyrin with band 3. a, Two orthogonal views of the atomic model of $B_4P_1A_1$ complex (ribbon), with density map in transparent gray. The density of the membrane domains of the second band 3 dimer are weak and visible only at a low density threshold, and are thus not modeled. **b**, Interaction between cdb3 and ankyrin from the $B_2P_1A_2$ complex. Residues of band 3 involved in ankyrin interaction are colored in red and labeled. Positions of the mutations used in **c** are indicated as dots. **c**, SDS-PAGE gel of the His-tag pull-down assay from the recombinant proteins. Band 3 mutations G130R and R155A eliminated ankyrin binding; ankyrin truncations (ARs 18–24, ARs 19–24 and ARs 20–24) and the mutations on AR-19 (Q623A and Y624A) abolished band 3 interaction. The experiments were repeated independently three times, and representative results are shown here.

interaction. Earlier, site-directed mutagenesis and antibody studies indicated that residues 63–73 (ref. [42]), 118–162 (ref. [9]) and 175–185 (ref. [42]) in the peripheral region of cdb3 were responsible for ankyrin binding. Site-directed spin-labeling on ankyrin demonstrated that its convex surface, rather than its concave groove of ARs 18–20, served as primary sites to contact cdb3 (ref. [11]), which is consistent with our structures.

As indicated above, the protein-4.2 binding sites on band 3 partially overlap with the ankyrin binding sites on band 3 (Extended Data Fig. 6), indicating that protein 4.2 and ankyrin associate with band 3 monomer exclusively. The interface between protein 4.2 and ankyrin spans about 1,630 Å^2, which is ~2.4-fold larger than the interface of band 3 and ankyrin (about 690 Å^2). Combined with the described interactions between protein 4.2 and band 3 in the previous section, it can be inferred that protein 4.2 may function as a linker to strengthen the ankyrin–band 3 association, consistent with previous findings that protein 4.2 deficiency weakened ankyrin–band 3 association on the erythrocyte membrane[30,43,44].

Discussion

Prior biochemical analysis of band 3 multiprotein complex assembly during erythropoiesis established the temporal progression towards the assembly of the ankyrin complex from various subcomplexes, including band 3, band 3–protein 4.2 complex and Rh complex[44–46]. The ratio of abundance of band 3, protein 4.2 and ankyrin in RBCs is about 10:2:1 (ref. [47]), which differs from the stoichiometry ratio (4:1:1) of these proteins in the ankyrin complex. Therefore, as the most abundant protein on the mature RBC membrane[48], band 3 could exist as a dimer without forming larger complexes with others in the mature RBC; likewise, other subcomplexes could exist without forming the ultimate supra-complex with all components. Indeed, their existence on mature RBCs is the basis for our ability to use the stepwise fractionation strategy to capture a total of nine native structures from the RBC membrane reported above, although we could not rule out the possibility that some may have resulted from disassembly during isolation. These results now allow us to populate the previously depicted model of ankyrin complex assembly (Fig. 5 and Supplementary Video 1) during erythropoiesis with experimentally observed subcomplex structures.

Assembly of the ankyrin complex possibly starts from free band 3 dimer[46]. By interacting with the rev-V-shaped band 3, protein 4.2 is incorporated to form the band 3–protein 4.2 complex, first in a loosely bound vertical conformation ($B_2P_1^{loose}$, Fig. 5 step 1) and then converted into a tightly bound vertical conformation ($B_2P_1^{vertical}$) (Fig. 5 step 2 and Extended Data Fig. 3c). A second protein 4.2 molecule can further interact with the unoccupied cdb3, forming a $B_2P_2^{vertical}$ complex with C_2 symmetry (Fig. 5 step 2a). Next, the membrane anchorage site of protein 4.2 moves from the edge to the center of the mdb3 dimer, while cdb3 shifts off the twofold axis (Extended Data Fig. 9a–e), transitioning from $B_2P_1^{vertical}$ into $B_2P_1^{diagonal}$ (Fig. 5 step 3). Protein 4.2 interacts with the CM-linker of band 3 in $B_2P_1^{diagonal}$, further stabilizing the diagonal conformation of protein 4.2 in the band 3–protein 4.2 complex (Extended Data Fig. 9f–h). Following the formation of $B_2P_1^{diagonal}$, one ankyrin molecule binds to protein 4.2, resulting in the $B_2P_1A_1$ complex (Fig. 5 step 4). By simultaneously interacting with protein 4.2 at ARs 6–13 and band 3 at ARs 17–20, ankyrin can bridge two band 3 dimers to form a $B_4P_1A_1$ complex (Fig. 5 step 5), consistent with our results from gel-filtration analysis of the reconstituted ankyrin complex (Extended Data Fig. 10b) and the observation that binding of ankyrin to band 3 promoted the formation of band 3 tetramers[49,50]. To align mdb3 of both band 3 dimers to the cell membrane, the second band 3 dimer must be in the V shape conformation and without protein 4.2 binding (Fig. 5 step 5).

Notably absent from the above assembly picture are several other complexes, likely owing to their flexibility and/or transient existence. For example, a second ankyrin molecule can bind to cdb3 not occupied by protein 4.2, forming a $B_2P_1A_2$ complex (Extended Data Fig. 10c), which constitutes a small portion (14% of the particles) of ankyrin-bound complexes. Analytic gel-filtration analysis of the reconstituted ankyrin complex shows that the second ankyrin (Extended Data Fig. 10d) can be incorporated into the ankyrin complex. Furthermore, through the interaction between the ZU5–UPA

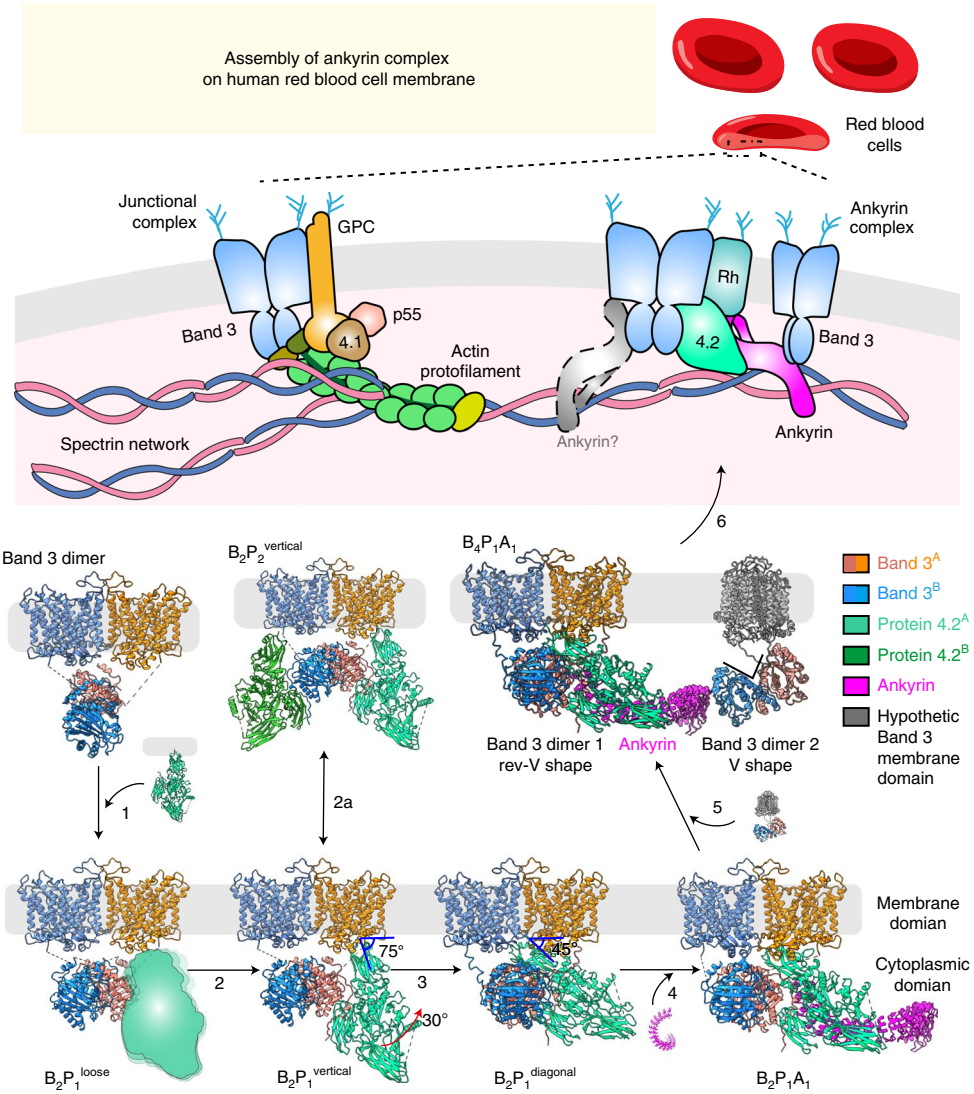

Fig. 5 | Schematic and possible assembly model of the ankyrin complex. Seven of the nine structures reported in the paper are depicted, each showing one possible assembly state (loosely bound protein 4.2 and complexes involving the second ankyrin molecule are shown as cartoon). For the $B_4P_1A_1$ complex, the membrane domains of the second band 3 dimer are hypothetically modeled (gray) to align to the membrane. Arrows depict possible directions of the assembly pathway, from the band 3 dimer to the ankyrin complex.

domain of ankyrin and repeats 13–14 of β-spectrin[51], the ankyrin complex links the spectrin network to the erythrocyte membrane (Fig. 5, step 6). Other complexes, such as the Rh complex, which contains RhCE, RhD, RhAG, CD47, LW and glycophorin B, can also interact with band 3, protein 4.2 and ankyrin[4,52], forming the intact ankyrin complex. While association of protein 4.2 and ankyrin with band 3 may occur at an early stage of erythropoiesis, even prior to membrane integration, incorporation of the Rh complex is thought to happen afterwards, on the cell membrane[45,46]. The validity of our proposed model of ankyrin complex assembly (Fig. 5) and other possible assembly intermediates during erythropoiesis await testing by cryo-electron tomography of erythropoiesis at different stages.

The importance of the current study lies in both biology and technology perspectives. From the biology perspective, mutations on the components of the ankyrin complex can result in disorders in erythrocytes (hereditary spherocytosis, South Asian ovalocytosis and hereditary stomatocytosis[5,6]) (Extended Data Fig. 10f). In hereditary spherocytosis, disruption of subunit interactions in the ankyrin complex results in loss of connection between the cytoskeleton and the membrane, consequently decreasing mechanical resistance and shortening the lifespan of the erythrocyte. Disease mutations, including G130R and E40K of band 3 and D145Y of protein 4.2, are located at the subunit binding interfaces. The availability of atomic structures of the ankyrin complex provides mechanic insight into RBC functions and paves the way for developing therapeutics against these diseases. From a technical perspective, the current work demonstrates an approach for direct visualization, at near-atomic resolution, of native protein complexes as they exist on membranes or in the cellular milieu. As such, notwithstanding the obvious challenges in dealing with species existing only transiently in cells, this approach opens the door for structural study of native macromolecular complexes to capture their multiple conformational states (for example, changes in binding partners[53] or cycling through subcomplexes like the spliceosome[54,55]) and during various functional stages (for example, genesis of RBCs in health and progression of pathology in diseases[56]).

Online content

Any methods, additional references, Nature Research reporting summaries, source data, extended data, supplementary information, acknowledgements, peer review information; details of

author contributions and competing interests; and statements of data and code availability are available at https://doi.org/10.1038/s41594-022-00779-7.

Received: 26 November 2021; Accepted: 14 April 2022;
Published online: 02 June 2022

References

1. Shi, J. et al. Engineered red blood cells as carriers for systemic delivery of a wide array of functional probes. *Proc. Natl Acad. Sci. USA* **111**, 10131–10136 (2014).
2. Bennett, V. & Baines, A. J. Spectrin and ankyrin-based pathways: metazoan inventions for integrating cells into tissues. *Physiol. Rev.* **81**, 1353–1392 (2001).
3. Bennett, V. & Stenbuck, P. J. The membrane attachment protein for spectrin is associated with band 3 in human erythrocyte membranes. *Nature* **280**, 468–473 (1979).
4. Mankelow, T. J., Satchwell, T. J. & Burton, N. M. Refined views of multi-protein complexes in the erythrocyte membrane. *Blood Cells Mol. Dis.* **49**, 1–10 (2012).
5. Narla, J. & Mohandas, N. Red cell membrane disorders. *Int J. Lab Hematol.* **39**(Suppl 1), 47–52 (2017).
6. Risinger, M. & Kalfa, T. A. Red cell membrane disorders: structure meets function. *Blood* **136**, 1250–1261 (2020).
7. Korsgren, C. & Cohen, C. M. Associations of human erythrocyte band 4.2. Binding to ankyrin and to the cytoplasmic domain of band 3. *J. Biol. Chem.* **263**, 10212–10218 (1988).
8. Kumpornsin, K., Jiemsup, S., Yongkiettrakul, S. & Chookajorn, T. Characterization of band 3–ankyrin–protein 4.2 complex by biochemical and mass spectrometry approaches. *Biochem. Biophys. Res. Commun.* **406**, 332–335 (2011).
9. Davis, L., Lux, S. E. & Bennett, V. Mapping the ankyrin-binding site of the human erythrocyte anion exchanger. *J. Biol. Chem.* **264**, 9665–9672 (1989).
10. Davis, L. H. & Bennett, V. Mapping the binding-sites of human erythrocyte ankyrin for the anion-exchanger and spectrin. *J. Biol. Chem.* **265**, 10589–10596 (1990).
11. Kim, S. et al. Determination of structural models of the complex between the cytoplasmic domain of erythrocyte band 3 and ankyrin-R repeats 13–24. *J. Biol. Chem.* **286**, 20746–20757 (2011).
12. Risinger, M. A., Dotimas, E. M. & Cohen, C. M. Human erythrocyte protein 4.2, a high copy number membrane protein, is N-myristylated. *J. Biol. Chem.* **267**, 5680–5685 (1992).
13. Toye, A. M. et al. Protein-4.2 association with band 3 (AE1, SLCA4) in *Xenopus* oocytes: effects of three natural protein-4.2 mutations associated with hemolytic anemia. *Blood* **105**, 4088–4095 (2005).
14. Korsgren, C., Lawler, J., Lambert, S., Speicher, D. & Cohen, C. M. Complete amino acid sequence and homologies of human erythrocyte membrane protein band 4.2. *Proc. Natl Acad. Sci. USA* **87**, 613–617 (1990).
15. Zhang, D., Kiyatkin, A., Bolin, J. T. & Low, P. S. Crystallographic structure and functional interpretation of the cytoplasmic domain of erythrocyte membrane band 3. *Blood* **96**, 2925–2933 (2000).
16. Arakawa, T. et al. Crystal structure of the anion exchanger domain of human erythrocyte band 3. *Science* **350**, 680–684 (2015).
17. Michaely, P., Tomchick, D. R., Machius, M. & Anderson, R. G. Crystal structure of a 12 ANK repeat stack from human ankyrinR. *EMBO J.* **21**, 6387–6396 (2002).
18. Stark, H. GraFix: stabilization of fragile macromolecular complexes for single particle cryo-EM. *Methods Enzymol.* **481**, 109–126 (2010).
19. De Vecchis, D., Reithmeier, R. A. F. & Kalli, A. C. Molecular simulations of intact anion exchanger 1 reveal specific domain and lipid interactions. *Biophys. J.* **117**, 1364–1379 (2019).
20. Wang, D. N. Band 3 protein: structure, flexibility and function. *FEBS Lett.* **346**, 26–31 (1994).
21. Jiang, J. et al. Single particle electron microscopy analysis of the bovine anion exchanger 1 reveals a flexible linker connecting the cytoplasmic and membrane domains. *PLoS ONE* **8**, e55408 (2013).
22. Romero, M. F., Chen, A. P., Parker, M. D. & Boron, W. F. The SLC4 family of bicarbonate (HCO_3^-) transporters. *Mol. Asp. Med* **34**, 159–182 (2013).
23. Wang, W. et al. Cryo-EM structure of the sodium-driven chloride/bicarbonate exchanger NDCBE. *Nat. Commun.* **12**, 5690 (2021).
24. Yu, X. et al. Dimeric structure of the uracil:proton symporter UraA provides mechanistic insights into the SLC4/23/26 transporters. *Cell Res* **27**, 1020–1033 (2017).
25. Wang, C. et al. Structural mechanism of the active bicarbonate transporter from cyanobacteria. *Nat. Plants* **5**, 1184–1193 (2019).
26. Muller-Berger, S. et al. Roles of histidine 752 and glutamate 699 in the pH dependence of mouse band 3 protein-mediated anion transport. *Biochemistry* **34**, 9325–9332 (1995).
27. Chernova, M. N. et al. Electrogenic sulfate/chloride exchange in *Xenopus* oocytes mediated by murine AE1 E699Q. *J. Gen. Physiol.* **109**, 345–360 (1997).
28. Karbach, D., Staub, M., Wood, P. G. & Passow, H. Effect of site-directed mutagenesis of the arginine residues 509 and 748 on mouse band 3 protein-mediated anion transport. *Biochim. Biophys. Acta* **1371**, 114–122 (1998).
29. Bork, P., Holm, L. & Sander, C. The immunoglobulin fold. Structural classification, sequence patterns and common core. *J. Mol. Biol.* **242**, 309–320 (1994).
30. Satchwell, T. J., Shoemark, D. K., Sessions, R. B. & Toye, A. M. Protein 4.2: a complex linker. *Blood Cells Mol. Dis.* **42**, 201–210 (2009).
31. Ahvazi, B., Kim, H. C., Kee, S. H., Nemes, Z. & Steinert, P. M. Three-dimensional structure of the human transglutaminase 3 enzyme: binding of calcium ions changes structure for activation. *EMBO J.* **21**, 2055–2067 (2002).
32. Yee, V. C. et al. Three-dimensional structure of a transglutaminase: human blood coagulation factor XIII. *Proc. Natl Acad. Sci. USA* **91**, 7296–7300 (1994).
33. Azim, A. C. et al. Human erythrocyte dematin and protein 4.2 (pallidin) are ATP binding proteins. *Biochemistry* **35**, 3001–3006 (1996).
34. Risinger, M. A., Dotimas, E. M. & Cohen, C. M. Human erythrocyte protein 4.2, a high copy number membrane-protein, Is N-myristylated. *J. Biol. Chem.* **267**, 5680–5685 (1992).
35. Malik, S., Sami, M. & Watts, A. A role for band 4.2 in human erythrocyte band 3 mediated anion transport. *Biochemistry* **32**, 10078–10084 (1993).
36. Steck, T. L. & Yu, J. Selective solubilization of proteins from red blood cell membranes by protein perturbants. *J. Supramol. Struct.* **1**, 220–232 (1973).
37. Korsgren, C. & Cohen, C. M. Purification and properties of human erythrocyte band 4.2. Association with the cytoplasmic domain of band 3. *J. Biol. Chem.* **261**, 5536–5543 (1986).
38. Rybicki, A. C. et al. Human erythrocyte protein 4.2 deficiency associated with hemolytic anemia and a homozygous 40glutamic acid → lysine substitution in the cytoplasmic domain of band 3 (band 3Montefiore). *Blood* **81**, 2155–2165 (1993).
39. Inoue, T. et al. Homozygous missense mutation (band 3 Fukuoka: G130R): a mild form of hereditary spherocytosis with near-normal band 3 content and minimal changes of membrane ultrastructure despite moderate protein 4.2 deficiency. *Br. J. Haematol.* **102**, 932–939 (1998).
40. Wang, C. et al. Structural basis of diverse membrane target recognitions by ankyrins. *eLife* **3**, e04353 (2014).
41. Bhattacharyya, R. et al. Mapping of a palmitoylatable band 3-binding domain of human erythrocyte membrane protein 4.2. *Biochem. J.* **340**, 505–512 (1999).
42. Grey, J. L., Kodippili, G. C., Simon, K. & Low, P. S. Identification of contact sites between ankyrin and band 3 in the human erythrocyte membrane. *Biochemistry* **51**, 6838–6846 (2012).
43. Rybicki, A. C., Schwartz, R. S., Hustedt, E. J. & Cobb, C. E. Increased rotational mobility and extractability of band 3 from protein 4.2-deficient erythrocyte membranes: evidence of a role for protein 4.2 in strengthening the band 3-cytoskeleton linkage. *Blood* **88**, 2745–2753 (1996).
44. van den Akker, E. et al. Investigating the key membrane protein changes during in vitro erythropoiesis of protein 4.2 (-) cells (mutations Chartres 1 and 2). *Haematologica* **95**, 1278–1286 (2010).
45. Satchwell, T. J. et al. Severe Ankyrin-R deficiency results in impaired surface retention and lysosomal degradation of RhAG in human erythroblasts. *Haematologica* **101**, 1018–1027 (2016).
46. Satchwell, T. J. et al. Critical band 3 multiprotein complex interactions establish early during human erythropoiesis. *Blood* **118**, 182–191 (2011).
47. Burton, N. M. & Bruce, L. J. Modelling the structure of the red cell membrane. *Biochem. Cell Biol.* **89**, 200–215 (2011).
48. Low, P. S. Structure and function of the cytoplasmic domain of band 3: center of erythrocyte membrane-peripheral protein interactions. *Biochim. Biophys. Acta* **864**, 145–167 (1986).
49. Van Dort, H. M., Moriyama, R. & Low, P. S. Effect of band 3 subunit equilibrium on the kinetics and affinity of ankyrin binding to erythrocyte membrane vesicles. *J. Biol. Chem.* **273**, 14819–14826 (1998).
50. Yi, S. J. et al. Red cell membranes of ankyrin-deficient nb/nb mice lack band 3 tetramers but contain normal membrane skeletons. *Biochemistry* **36**, 9596–9604 (1997).
51. Ipsaro, J. J. & Mondragon, A. Structural basis for spectrin recognition by ankyrin. *Blood* **115**, 4093–4101 (2010).
52. Bruce, L. J. et al. A band 3-based macrocomplex of integral and peripheral proteins in the RBC membrane. *Blood* **101**, 4180–4188 (2003).
53. Ho, C. M. et al. Malaria parasite translocon structure and mechanism of effector export. *Nature* **561**, 70–75 (2018).
54. Liu, S. et al. Structure of the yeast spliceosomal postcatalytic P complex. *Science* **358**, 1278–1283 (2017).
55. Yan, C., Wan, R., Bai, R., Huang, G. & Shi, Y. Structure of a yeast step II catalytically activated spliceosome. *Science* **355**, 149–155 (2017).
56. Fitzpatrick, A. W. P. et al. Cryo-EM structures of tau filaments from Alzheimer's disease. *Nature* **547**, 185–190 (2017).

Publisher's note Springer Nature remains neutral with regard to jurisdictional claims in published maps and institutional affiliations.

© The Author(s), under exclusive licence to Springer Nature America, Inc. 2022

Methods

Protein purification. To dislodge different band-3-associated complexes from the human RBC membrane–cytoskeleton network, ghost membrane was sequentially treated with low-salt and high-salt buffers as reported before[8,57] (Extended Data Fig. 1a). Briefly, 50 mL packed human red blood cells (BioIVT) at 4 °C were washed with five volumes of phosphate-buffered saline (PBS) at 2,000*g* for 10 min. All the following steps were performed at 4 °C, unless otherwise specified. The cells were then lysed in 10 volumes of hypotonic buffer containing 7.5 mM sodium phosphate at pH 7.5, 1 mM EDTA and protease inhibitors (0.5 mM phenylmethylsulphonyl fluoride (PMSF), 0.7 μg/mL pepstatin A, 2.5 μg/mL aprotinin, 5 μg/mL leupeptin) for 30 min. The lysate was centrifuged for 30 min at 20,000*g* to pellet the ghost membrane. The ghost membrane was further washed in the hypotonic buffer and pelleted at 20,000*g* for 30 min 4 times, followed by extraction in a low-salt buffer containing 0.1 M KCl, 7.5 mM sodium phosphate at pH 7.5, 1 mM EDTA, 1 mM dithiothreitol (DTT), 1% *N*-dodecyl-β-maltoside (DDM) and protease inhibitors for 1 h. Subsequently, the sample was centrifuged at 20,000*g* for 20 min, resulting in the supernatant (low-salt fraction) and the pellet. The pellet was further extracted with a high-salt buffer containing 1 M KCl, 7.5 mM sodium phosphate at pH 7.5, 1 mM EDTA, 1 mM DTT, 1% DDM and protease inhibitors for 1 h. After centrifugation at 45,000*g* for 30 min, the supernatant (high-salt fraction) was obtained for further purification.

The low-salt and high-salt fractions were further purified using a gel-filtration column Superose 6 Increase 10/300 GL (GE Healthcare). The low-salt fraction was injected into the column in SEC150 buffer (10 mM Tris 7.5, 150 mM NaCl, 1 mM DTT, 0.015% DDM and protease inhibitors). After analysis by SDS-PAGE, band 3 fractions were pooled and purified using the same column for a second time (Extended Data Fig. 1b). The peak fraction was concentrated and used for cryo-EM grid preparation. The high-salt fraction was injected into the gel-filtration column in SEC500 buffer (10 mM Tris 7.5, 500 mM NaCl, 1 mM DTT, 0.015% DDM and protease inhibitor), resulting in an elution volume of 14.5 mL of high-salt fraction 1 (band 3–protein 4.2 complex) and 12.5 mL of high-salt fraction 2 (ankyrin complex) (Extended Data Fig. 1c). Band 3–protein 4.2 complex was pooled and further purified by using the same column for a second time in SEC300 buffer (10 mM Tris 7.5, 300 mM NaCl, 1 mM DTT, 0.015% DDM and protease inhibitor) (Extended Data Fig. 1d). The good fractions were combined and concentrated for cryo-EM. For band 3–protein 4.2 complex used in analytical gel filtration, pooled fractions from the first gel-filtration purification were further purified by an anion exchange column (Source-15Q, GE Healthcare) and were then subjected to a second gel-filtration column in SEC150 buffer. The ankyrin complex was stabilized by a Grafix[18,58] method after the first gel-filtration purification of the high-salt fraction. The glycerol gradient was made by mixing 6 mL light buffer (20 mM HEPES 7.5, 300 mM NaCl, 0.015% DDM, 10% glycerol) and 6 mL heavy buffer (20 mM HEPES 7.5, 300 mM NaCl, 0.015% DDM, 30% glycerol, 0.2% glutaraldehyde (Polysciences)) in a gradient master (BioComp). Ankyrin complex was concentrated to 200 μL and dialyzed to buffer containing 20 mM HEPES 7.5, 300 mM NaCl, 0.015% DDM. The sample was loaded on top of the glycerol gradient and centrifuged at 4 °C for 18 h at a speed of 210,000 g in SW-41Ti rotor (Beckman). Fractions of 500 μL were collected, and the cross-link reaction was quenched by adding Tris 7.5 to a final concentration of 50 mM. Good fractions after negative stain screening were combined and subjected to the gel-filtration column in SEC300 buffer (Extended Data Fig. 1e). Finally, the fractions in the 12.5-mL peak were collected and used for cryo-EM.

All recombinant proteins and mutants were overexpressed in *Escherichia coli* strain BL21(DE3). DNA sequences encoding ankyrin ARs 1–24 (aa 1–827), ARs 13–24 (aa 402–827), ARs 16–24 (aa 494–827), ARs 17–24 (aa 527–827), ARs 18–24 (aa 561–827), ARs 19–24 (aa 597–827), ARs 20–24 (aa 630–827) and band 3 cytoplasmic domain (aa 1–379) were cloned into a modified pET-28a vector with an N-terminal hexahistidine tag followed by a SUMO tag. Mutants were generated by QuikChange mutagenesis and confirmed by DNA sequencing. Proteins were expressed in *E. coli* and induced with 0.5 mM isopropyl-β-D-thiogalactoside (IPTG, Sigma) at an OD_{600} of 0.8. The culture was incubated at 25 °C overnight. Cells were collected by centrifugation and resuspended in a buffer containing 20 mM Tris 7.5, 300 mM NaCl, 1 mM PMSF and 1 mM benzamidine. The suspensions were lysed by using a cell disruptor (Avestin). After high-speed centrifugation at 30,000*g* for 1 h, the supernatant was loaded to a column with HisPur cobalt resin (Thermo Fisher). After a wash step, proteins were eluted with a buffer containing 20 mM Tris 7.5, 150 mM NaCl,1 mM benzamidine and 250 mM imidazole. For band 3 cytoplasmic domain, the His_6-SUMO tag was removed by ULP1 (a SUMO protease). For all the ankyrin constructs, the His_6-SUMO tag was retained. Proteins were further purified by ion-exchange column (Source-15Q, GE healthcare) and polished by gel-filtration column (Superdex-200, GE Healthcare) in SEC150 buffer without protease inhibitors. The purified proteins were concentrated and stored at −80 °C.

Cryo-EM sample preparation and image acquisition. For cryo-EM sample optimization, an aliquot of 3 μL of sample was applied onto a glow-discharged holey carbon-coated copper grid (300 mesh, QUANTIFOIL R 2/1) or holey gold grid (300 mesh, UltrAuFoils R 1.2/1.3). The grid was blotted with Grade 595 filter paper (Ted Pella) and flash-frozen in liquid ethane with an FEI Mark IV Vitrobot. An FEI TF20 cryo-EM instrument was used to screen grids. Cryo-EM grids with optimal particle distribution and ice thickness were obtained by varying the gas source (air using PELCO easiGlow, target vacuum of 0.37 mbar, target current of 15 mA; or H_2/O_2 using Gatan Model 950 advanced plasma system, target vacuum of 70 mTorr, target power of 50 W) and time for glow discharge, the volume of applied samples, chamber temperature and humidity, blotting time and force, and drain time after blotting. Our best grids for the low-salt fraction were obtained with holey carbon-coated copper grids, 20 s glow discharge using H_2/O_2 and with the Vitrobot sample chamber temperature set at 8 °C, 100% humidity, 6 s blotting time, 3 blotting force and 0 s drain time. The best grids for high-salt fractions 1 and 2 were obtained with holey gold grids, 20 s glow discharge using H_2/O_2 and with the Vitrobot sample chamber set at 8 °C temperature, 100% humidity, 6 s blotting time, 3 blotting force and 0 s drain time.

Optimized cryo-EM grids were loaded into an FEI Titan Krios electron microscope with a Gatan Imaging Filter (GIF) Quantum LS device and a post-GIF K2 or K3 Summit direct electron detector. The microscope was operated at 300 kV with the GIF energy-filtering slit width set at 20 eV. Movies were acquired using SerialEM[59] by electron counting in super-resolution mode at a pixel size of 0.535 Å/pixel or 0.55 Å/pixel with a total dosage of ~50 $e^-/Å^2$/movie. Image conditions are summarized in Table 1.

Cryo-EM reconstruction. Frames in each movie were aligned for drift correction with the GPU-accelerated program MotionCor2 (ref. [60]). Two averaged micrographs, one with dose weighting and the other without, were generated for each movie after drift correction. The averaged micrographs have a calibrated pixel size of 1.062 Å (low-salt fraction) or 1.1 Å (high-salt fraction 1 and 2) at the specimen scale. The averaged micrographs without dose weighting were used only for defocus determination, and the averaged micrographs with dose weighting were used for all other steps of image processing. Workflows are summarized in Extended Data Figs. 2, 3 and 4 for the low-salt fraction and high-salt fraction 1 and high-salt fraction 2, respectively.

For the low-salt fraction (band 3), a total of 9,455 averaged micrographs were obtained, of which 1,000 were subjected to a quick analysis in cryoSPARC v3 (ref. [61]). The defocus values of the 9,455 averaged micrographs were determined by CTFFIND4 (ref. [62]); 2,658,315 particles were automatically picked without reference using Gautomatch (https://www2.mrc-lmb.cam.ac.uk/research/locally-developed-software/zhang-software/). Several rounds of reference-free 2D classification were subsequently performed in RELION3.1 (refs. [63,64]) to remove 'bad' particles (that is, classes with fuzzy or un-interpretable features), yielding 961,892 good particles. To retrieve more real particles from the micrographs, Topaz[65], a convolutional neural-network-based particle-picking software, was trained by the final coordinates from cryoSPARC and used for the second round of particle picking; 2,953,637 particles were obtained initially and resulted in 976,060 good particles after rounds of 2D classification in RELION. After the two sets of particles were combined and duplicates removed, a total of 1,286,729 particles were collected. A global search 3D classification in RELION was performed, with the map from cryoSPARC as the initial model. One good class containing 530,179 particles was selected and subjected to a final step of 3D auto-refinement in RELION. The membrane part and cytoplasmic part of band 3 are refined together, without local refinement. The two half-maps from this auto-refinement step were subjected to RELION's standard post-processing procedure, yielding a final map with an average resolution of 4.8 Å.

For high-salt fraction 1 (band 3–protein 4.2 complex), a total of 20,842 averaged micrographs was obtained and subjected to particle picking in Gautomatch. Then, 2,031,749 particles were selected after 2D and 3D classification in RELION. The coordinates of the selected particles were used for Topaz training in the second round of particle picking, and 2,879,888 particles were selected after the second round of particle sorting. The two sets of selected particles were combined and duplicates were removed, resulting in 3,864,165 particles. These particles were subjected to a global search 3D classification with $K=5$, resulting in 4 structures of the band 3–protein 4.2 complex: 1,048,826 particles (27.1%) in the class of band 3 with a loosely bound protein 4.2 ($B_2P_1^{loose}$), 406,951 particles (10.5%) in the class of band 3 with protein 4.2 binding vertically ($B_2P_1^{vertical}$), 246,059 particles (6.4%) in the class of band 3 with two protein 4.2 binding vertically ($B_2P_2^{vertical}$) and 2,162,329 particles (56%) in the major class of band 3 with protein 4.2 binding diagonally ($B_2P_1^{diagonal}$). The $B_2P_1^{loose}$ complex, $B_2P_1^{vertical}$ complex and $B_2P_2^{vertical}$ complex were further 3D classified with the skip-align option in RELION and reconstructed to 4.1 Å, 4.6 Å and 4.6 Å, respectively. For the $B_2P_1^{diagonal}$ complex, the structure was classified and refined to 3.6 Å with an overall mask. When masks for the cytoplasmic part and the membrane part were applied, the structures of the cytoplasmic part and the membrane part were reconstructed to 3.1 Å and 3.3 Å, respectively.

For high-salt fraction 2 (ankyrin complex), 21,187 good micrographs were obtained. Using a strategy similar to that of the band 3 dataset, a total of 4,048,034 unique particles were collected after two rounds of particle picking and 2D classification. The selected particles were subjected to 2D and 3D classification, and one good class containing 593,880 particles was selected. To further increase the number of good particles, a method of seed-facilitated 3D classification[66] was used. Briefly, all the raw particles from autopick were divided into six subsets and then mixed with the good particles (seed) from the previous step of 3D classification. Subsequently, after applying 3D classification separately, all the good classes were

collected and combined, followed by 2D and 3D classification to generate a total of 1,410,445 good particles. These particles were further 3D classified into four classes, resulting in two structures, with 383,995 particles in $B_2P_1A_1$ complex (one ankyrin molecule binds to one $B_2P_1^{diagonal}$ complex via protein 4.2) and 63,084 particles in $B_2P_1A_2$ complex (two ankyrin molecules bind to one $B_2P_1^{diagonal}$ complex via protein 4.2 and band 3, respectively). The two complexes were classified and refined in cryoSPARC using non-uniform refinement to resolutions of 4.4 Å and 5.7 Å for $B_2P_1A_1$ complex (160,406 particles) and $B_2P_1A_2$ complex (34,612 particles), respectively. A further step of focused refinement improved the core region's resolutions to 4.1 Å and 4.6 Å for $B_2P_1A_1$ complex and $B_2P_1A_2$ complex, respectively. When lowering the threshold of the maps, smeared density emerges at the edges of the box, indicating that the box size of 384 pixels is not big enough to include all the densities. Therefore, these particles were re-centered and extracted in a box size of 560 pixels. After 3D classification and refinement, two structures of ankyrin-containing complex were reconstructed to 5.6 Å and 8.5 Å for $B_4P_1A_1$ complex and $(B_2P_1A_1)_2$ complex, respectively.

Resolution assessment. All resolutions reported above are based on the 'gold standard' FSC 0.143 criterion[67]. FSC curves were calculated using soft spherical masks, and high-resolution noise substitution was used to correct for convolution effects of the masks on the FSC curves[67]. Prior to visualization, all maps were sharpened by applying a negative B factor, estimated using automated procedures[67]. Local resolution was estimated using ResMap[68]. The overall quality of the maps for band 3, band 3–protein 4.2 complexes and ankyrin-containing complexes is presented in Extended Data Figs. 2d–f, 3d–h and 4d–f, respectively. The reconstruction statistics are summarized in Table 1.

Atomic modeling, model refinement and graphics visualization. Atomic-model building started from the $B_2P_1^{diagonal}$ complex map, which had the best resolution. We took advantage of the reported crystal structure of mdb3 (PDB: 4YZF)[16], which was fitted into the focus-refined membrane domain map (3.3 Å) by UCSF Chimera[69]. We manually adjusted its side chain conformation and, when necessary, moved the main chains to match the density map using Coot[70]. This allowed us to identify extra densities for loop N554-P566, loop A641-W648 and *N*-acetylglucosamine (NAG) close to residue N642, as well as lipids at the dimer interface that were tentatively assigned as DDM or cholesterol accordingly. For the cytoplasmic part, the crystal structure of cdb3 (PDB: 1HYN)[15] was fitted into the focus-refined cytoplasmic domain map (3.1 Å) and manually adjusted. This enabled us to identify the extra densities for the N terminus of the cdb3 (aa 30–55), absent in the crystal structure and interacting with protein 4.2 in our $B_2P_1^{diagonal}$ complex. Next, we built the atomic model for protein 4.2 de novo. Protein sequence assignment was mainly guided by visible densities of amino acid residues with bulky side chains, such as Trp, Tyr, Phe and Arg. Other residues including Gly and Pro also helped the assignment process. Unique patterns of sequence segments containing such residues were utilized for validation of residue assignment. Finally, the models of the membrane part and the cytoplasmic part were docked into the 3.6 Å overall map in Chimera. As the map resolution of the CM-linker between cdb3 and mdb3 is insufficient for de novo atomic modeling, we traced the main chain using Coot for aa 350–369.

For the structure of the band 3 dimer, models of cdb3 and mdb3 from the $B_2P_1^{diagonal}$ complex were fitted into the cryo-EM map in Chimera and manually adjusted using Coot. For the structures of $B_2P_1^{vertical}$ and $B_2P_2^{vertical}$, models of mdb3, cdb3 and protein 4.2 from the $B_2P_1^{diagonal}$ complex were docked and manually adjusted.

For the structure of the $B_2P_1A_1$ complex, we first docked the model of the $B_2P_1^{diagonal}$ complex into the cryo-EM map. Ankyrin repeats 6–20 (aa 174–658) with side chains were built de novo using the focus-refined map at 4.1 Å. ARs 21–24 were assigned with guidance from previous crystal structures of ankyrins (ARs 1–24 of AnkyrinB, PDB: 4RLV (ref. [40]); ARs 13–24 of AnkyrinR, PDB: 1N11 (ref. [17])) and truncated to Cβ owing to the lack of side chain densities. Next, the structure of $B_2P_1A_1$ complex was fitted into the maps of $B_2P_1A_2$. This enabled us to identify extra densities for a second ankyrin which directly interacts with band 3. The bulky side chains of the second ankyrin were built using the focus-refined map at 4.6 Å. The assignment of the band-3-associated ankyrin was further verified in both the $B_4P_1A_1$ and $(B_2P_1A_1)_2$ complexes.

The atomic models were refined using PHENIX[71] in real space with secondary structure and geometry restraints. All the models were also evaluated using the wwPDB validation server (Table 1). Representative densities are shown in Extended Data Figs. 2g, 3i and 4g,h. Visualization of the atomic models, including figures and movies, was accomplished in UCSF Chimera and Chimera X[69].

Structure-guided mutagenesis and pull-down assay. The pull-down assay was performed with HisPur cobalt resin at 4 °C in a binding buffer containing 10 mM Tris 7.5, 150 mM NaCl, 0.015% DDM. Twenty microliters of cobalt resin was used in a 200 µL binding reaction. Recombinant proteins were used in this assay. His_6-SUMO tagged ankyrin at a final concentration of 4 µM was pre-incubated with the resin and then mixed with 8 µM of band 3 cytoplasmic domain or mutant. After 60 min of incubation, the resin was washed 4 times with 1 mL of the binding buffer containing 10 mM imidazole and eluted with the binding buffer containing 250 mM imidazole. Samples were analyzed by SDS-PAGE and stained with InstantBlue (abcam). All experiments were repeated at least three times.

Analytical gel filtration. Analytical gel filtration chromatography was carried out with the Superose 6 Increase 10/300 GL column at 4 °C. The column was equilibrated with SEC150 buffer without protease inhibitors. Band 3–protein 4.2 complex was purified from the erythrocyte membrane. Ankyrin and band 3 cytoplasmic domain were purified from *E. coli*. The His_6-SUMO tag of ankyrin was retained. A protein sample of 500 µL was injected into the column and eluted at a flow rate of 0.5 mL/min. Fractions were then analyzed by SDS-PAGE.

Reporting summary. Further information on research design is available in the Nature Research Reporting Summary linked to this article.

Data availability

Cryo-EM density maps have been deposited in the Electron Microscopy Data Bank under accession numbers EMD-26148 (band 3 dimer), EMD-26145 ($B_2P_1^{loose}$), EMD-26146 ($B_2P_1^{vertical}$), EMD-26147 ($B_2P_2^{vertical}$), EMD-26142 ($B_2P_1^{diagonal}$), EMD-26143 (membrane part of $B_2P_1^{diagonal}$), EMD-26144 (cytoplasmic part of $B_2P_1^{diagonal}$), EMD-26149 ($B_2P_1A_1$), EMD-26150 (cytoplasmic part of $B_2P_1A_1$), EMD-26151 ($B_2P_1A_2$), EMD-26152 (focused refinement of $B_2P_1A_2$), EMD-26153 ($B_4P_1A_1$) and EMD-26154 ($(B_2P_1A_1)_2$). Model coordinates have been deposited in the Protein Data Bank under accession numbers 7TW2 (band 3 dimer), 7TW0 ($B_2P_1^{vertical}$), 7TW1 ($B_2P_2^{vertical}$), 7TVZ ($B_2P_1^{diagonal}$), 7TW3 ($B_2P_1A_1$), 7TW5 ($B_2P_1A_2$) and 7TW6 ($B_4P_1A_1$). Other structures used in this study were retrieved from the PDB with accession codes 4YZF for the crystal structure of band 3 membrane domain, 1HYN for the crystal structure of band 3 cytoplasmic domain, 1N11 for ARs 13–24 of ankyrinR, 4RLV for ARs 1–24 of ankyrinB, 1L9N for transglutaminase 3 and 6KI1 for BicA. All other data needed to evaluate the conclusions in the paper are present in the paper and/or the supplementary materials. Source data are provided with this paper.

References

57. Bennett, V. Isolation of an ankyrin-band 3 oligomer from human erythrocyte membranes. *Biochim. Biophys. Acta* **689**, 475–484 (1982).
58. Liu, X., Li, M., Xia, X., Li, X. & Chen, Z. Mechanism of chromatin remodelling revealed by the Snf2-nucleosome structure. *Nature* **544**, 440–445 (2017).
59. Mastronarde, D. N. Automated electron microscope tomography using robust prediction of specimen movements. *J. Struct. Biol.* **152**, 36–51 (2005).
60. Zheng, S. Q. et al. MotionCor2: anisotropic correction of beam-induced motion for improved cryo-electron microscopy. *Nat. Methods* **14**, 331–332 (2017).
61. Punjani, A., Rubinstein, J. L., Fleet, D. J. & Brubaker, M. A. cryoSPARC: algorithms for rapid unsupervised cryo-EM structure determination. *Nat. Methods* **14**, 290–296 (2017).
62. Rohou, A. & Grigorieff, N. CTFFIND4: fast and accurate defocus estimation from electron micrographs. *J. Struct. Biol.* **192**, 216–221 (2015).
63. Scheres, S. H. Processing of structurally heterogeneous cryo-EM data in RELION. *Methods Enzymol.* **579**, 125–157 (2016).
64. Scheres, S. H. RELION: implementation of a Bayesian approach to cryo-EM structure determination. *J. Struct. Biol.* **180**, 519–530 (2012).
65. Bepler, T. et al. Positive-unlabeled convolutional neural networks for particle picking in cryo-electron micrographs. *Nat. Methods* **16**, 1153–1160 (2019).
66. Wang, N. et al. Structural basis of human monocarboxylate transporter 1 inhibition by anti-cancer drug candidates. *Cell* **184**, 370–383 e13 (2021).
67. Rosenthal, P. B. & Henderson, R. Optimal determination of particle orientation, absolute hand, and contrast loss in single-particle electron cryomicroscopy. *J. Mol. Biol.* **333**, 721–745 (2003).
68. Kucukelbir, A., Sigworth, F. J. & Tagare, H. D. Quantifying the local resolution of cryo-EM density maps. *Nat. Methods* **11**, 63–65 (2014).
69. Pettersen, E. F. et al. UCSF Chimera—a visualization system for exploratory research and analysis. *J. Comput. Chem.* **25**, 1605–1612 (2004).
70. Emsley, P. & Cowtan, K. Coot: model-building tools for molecular graphics. *Acta Crystallogr D. Biol. Crystallogr* **60**, 2126–2132 (2004).
71. Adams, P. D. et al. PHENIX: a comprehensive Python-based system for macromolecular structure solution. *Acta Crystallogr D. Biol. Crystallogr* **66**, 213–221 (2010).
72. Madeira, F. et al. The EMBL-EBI search and sequence analysis tools APIs in 2019. *Nucleic Acids Res.* **47**, W636–W641 (2019).
73. Robert, X. & Gouet, P. Deciphering key features in protein structures with the new ENDscript server. *Nucleic Acids Res.* **42**, W320–W324 (2014).

Acknowledgements

We thank T. Nguyen, J. Zhen and A. Stevens for editorial assistance. This project is supported by grants from the US NIH (R01GM071940 to Z.H.Z.). We acknowledge the use of resources at the Electron Imaging Center for Nanomachines supported by UCLA

and grants from the NIH (1S10OD018111 and 1U24GM116792) and the National Science Foundation (DBI-1338135 and DMR-1548924).

Author contributions

Z.H.Z. conceived the project. X.X. and S.L. prepared samples and acquired and analyzed cryo-EM data. X.X. engineered and isolated the recombinant proteins and performed biochemistry analyses. S.L. and X.X. built the models. X.X., S.L. and Z.H.Z. interpreted the results and wrote the manuscript.

Competing interests

The authors declare no competing interests.

Additional information

Extended data is available for this paper at https://doi.org/10.1038/s41594-022-00779-7.

Supplementary information The online version contains supplementary material available at https://doi.org/10.1038/s41594-022-00779-7.

Correspondence and requests for materials should be addressed to Z. Hong Zhou.

Peer review information *Nature Structural and Molecular Biology* thanks Ash Toye, Yifan Cheng, and Werner KÄhlbrandt for their contribution to the peer review of this work. Primary Handling editor: Florian Ullrich, in collaboration with the Nature Structural & Molecular Biology team. Peer reviewer reports are available.

Reprints and permissions information is available at www.nature.com/reprints.

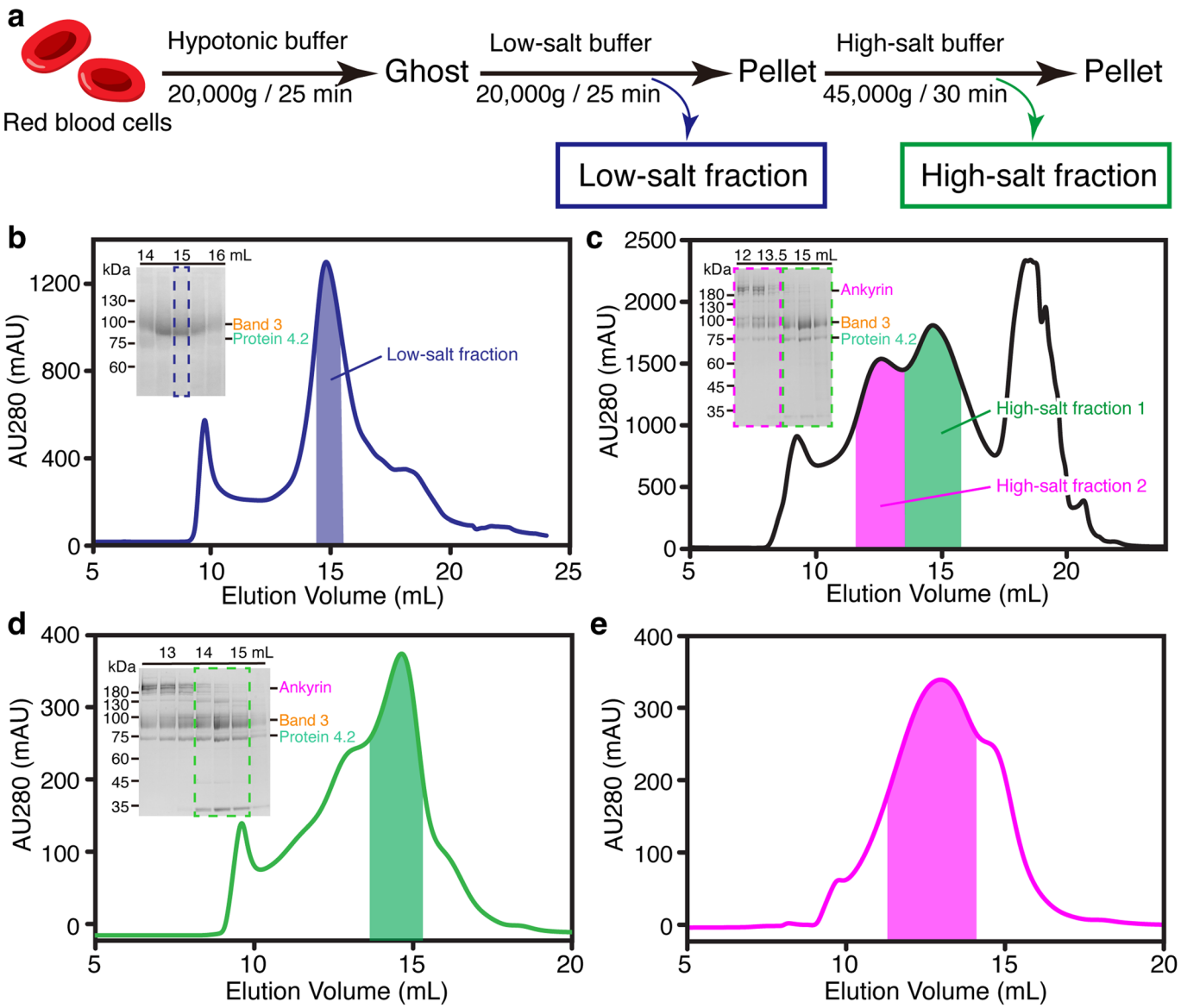

Extended Data Fig. 1 | Purification and cryo-EM reconstruction of the erythrocyte membrane proteins. (**a**) Workflow of the stepwise fractionation of erythrocyte membrane proteins. (**b**) The second gel-filtration chromatography profile of the low-salt fraction. The result from SDS-PAGE analysis of the peak fractions is inserted in the upper left corner. The peak fractions were applied to SDS-PAGE and visualized by Coomassie blue staining. Dashed blue box on the gel and blue bar on the chromatogram indicate the fractions collected for cryo-EM. (**c**) The first gel-filtration chromatography profile of the high-salt fraction. Green and magenta boxes on the gel and green and magenta bars on the chromatogram indicate the fractions collected for the protein 4.2 complex and ankyrin complex, respectively. (**d**) The second gel-filtration chromatography profile and corresponding gel of the protein 4.2 complex. Dashed green box on the gel and green bar on the chromatogram indicate the fractions collected for cryo-EM. (**e**) The gel-filtration chromatography profile of the ankyrin complex after Grafix purification. Magenta bar on the chromatogram indicates the fractions collected for cryo-EM.

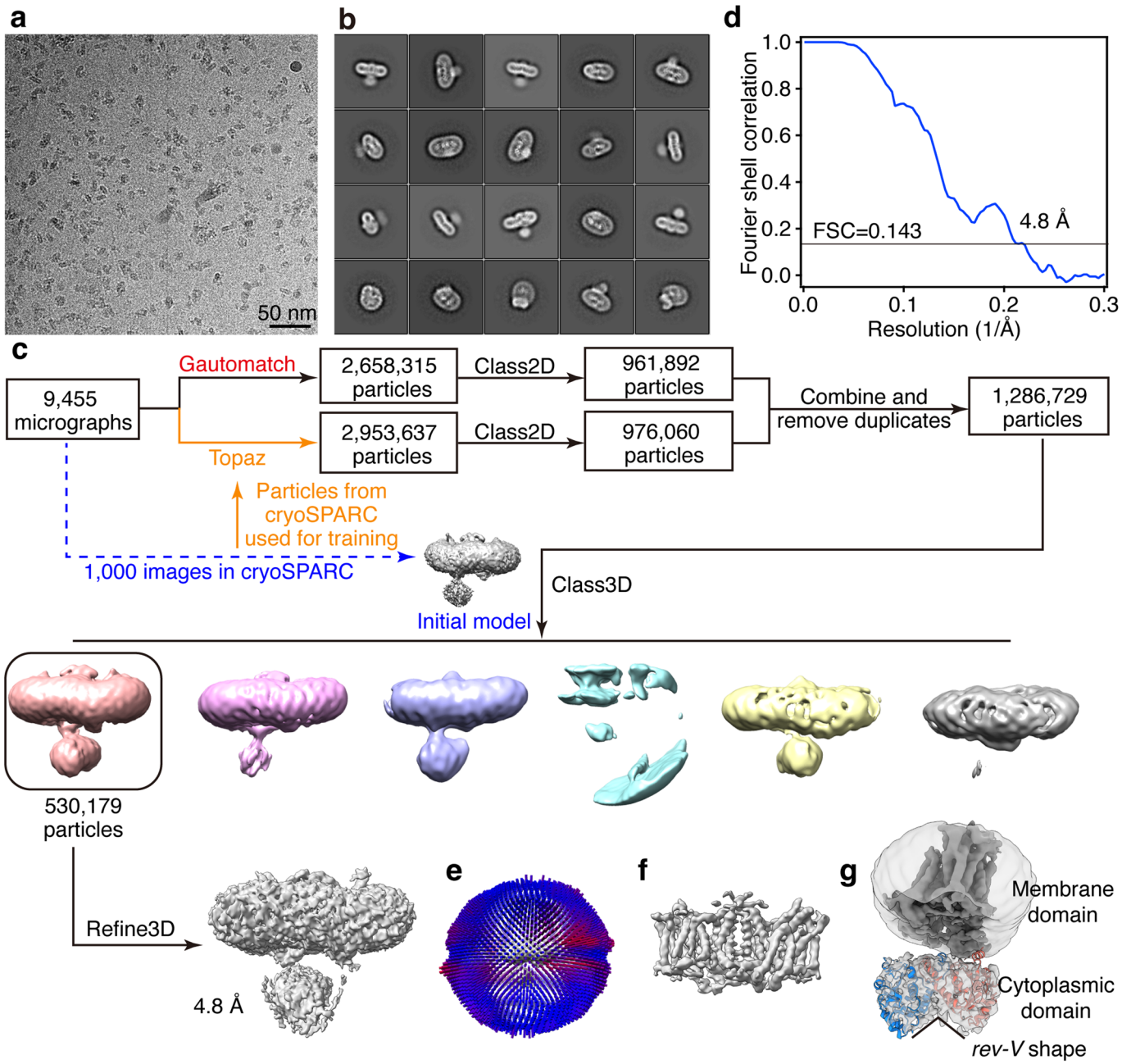

Extended Data Fig. 2 | Cryo-EM analysis of the low-salt fraction (band 3). (**a**) Representative cryo-EM image of the low-salt fraction from 9455 images collected. (**b**) Selected 2D class averages of the cryo-EM particle images. (**c**) Flow chart of cryo-EM data processing. (**d**) Gold-standard Fourier shell correlation (FSC) curve for 3D reconstruction. (**e**) Angular distribution of cryo-EM reconstructions used for final refinement. (**f**) Density of the membrane domain. (**g**) Atomic model of band 3 cytoplasmic domain fitted into the cryo-EM density. A lower map threshold is used in (g) compared to that of (f) to better present the cytoplasmic domain.

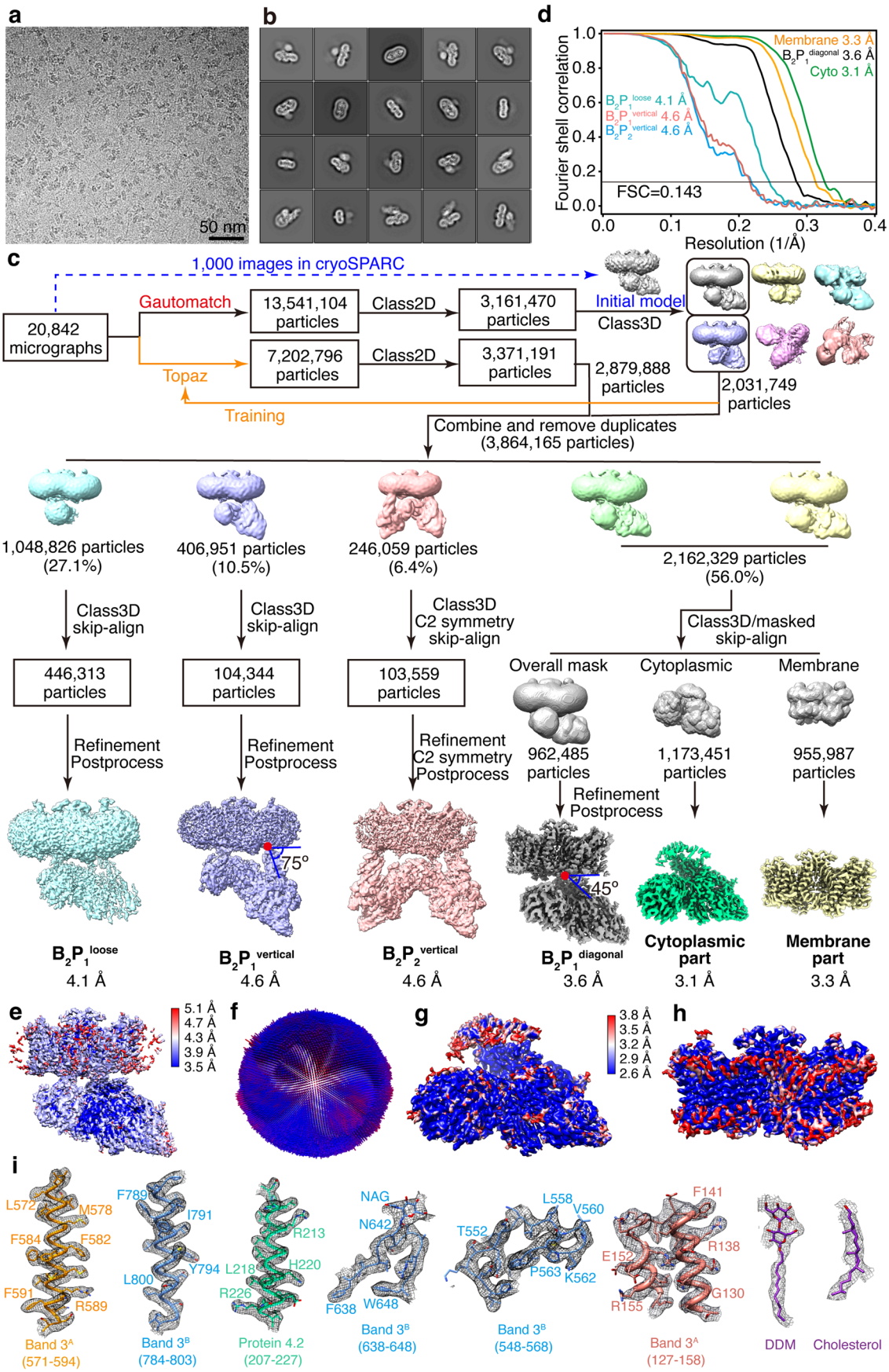

Extended Data Fig. 3 | See next page for caption.

Extended Data Fig. 3 | Image processing for the cryo-EM data of the high-salt fraction 1 (band 3-protein 4.2 complex). (**a**) Representative cryo-EM image of the high-salt fraction 1 from 20842 images collected. (**b**) Selected 2D class averages of the cryo-EM particle images. (**c**) Flow chart of cryo-EM data processing. (**d**), Gold-standard Fourier shell correlation (FSC) curves for 3D reconstructions. (**e**) Local resolution of the overall map of $B_2P_1^{diagonal}$ complex. (**f**) Angular distribution of cryo-EM reconstruction of $B_2P_1^{diagonal}$ complex used for final refinement. (**g-h**) Local resolutions of the focused refinement maps of the cytoplasmic part and membrane part of $B_2P_1^{diagonal\ complex}$. (**i**) Representative cryo-EM density maps of the $B_2P_1^{diagonal}$ complex.

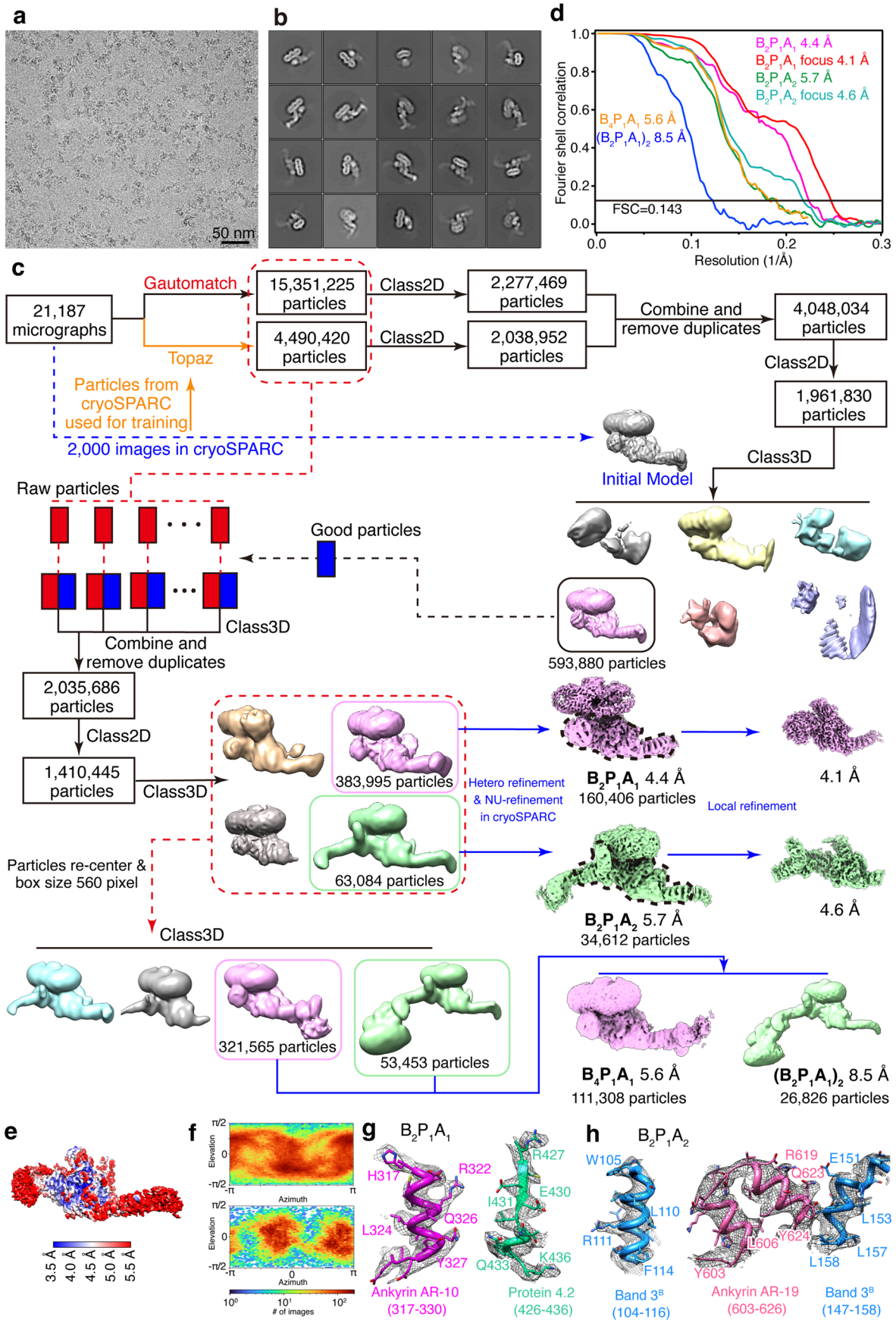

Extended Data Fig. 4 | See next page for caption.

Extended Data Fig. 4 | Cryo-EM analysis of the high-salt fraction 2 (ankyrin complex). (**a**) Representative cryo-EM image of the high-salt fraction 2 from 21187 images collected. (**b**) Selected 2D class averages of cryo-EM particle images. (**c**) Flow chart of cryo-EM data processing. (**d**) Gold-standard Fourier shell correlation (FSC) curves for 3D reconstructions. (**e**) Local resolution of the overall map of $B_2P_1A_1$ complex. **(f**) Angular distribution of cryo-EM reconstruction of $B_2P_1A_1$ complex. (**g**) Representative cryo-EM density maps of the $B_2P_1A_1$ complex showing the fragments of ankyrin and protein 4.2 at their binding interface. **(h**) Representative cryo-EM density maps of the $B_2P_1A_2$ complex showing the fragments of ankyrin and band 3 at their binding interface.

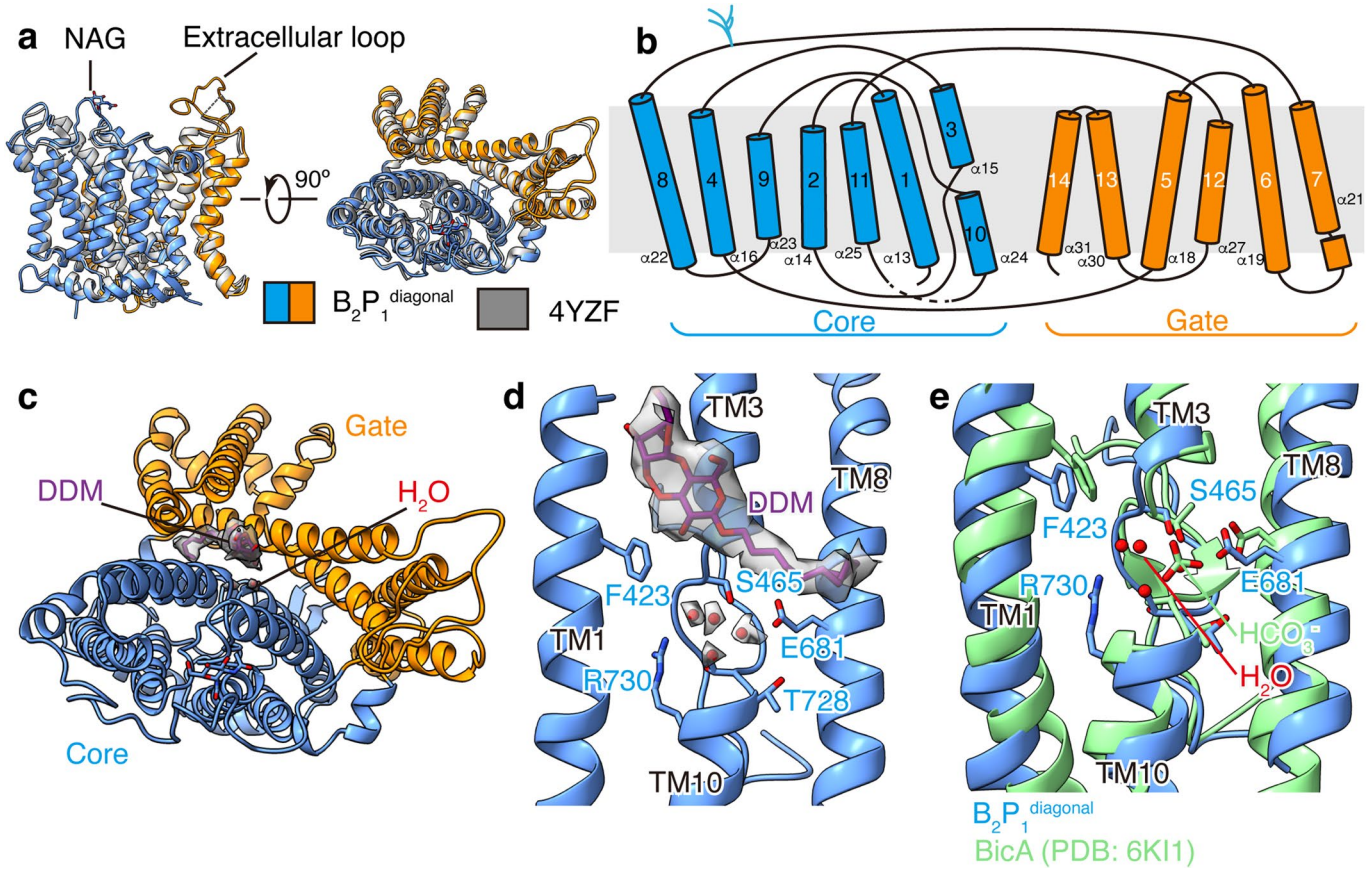

Extended Data Fig. 5 | Structural analysis of the band 3 membrane domain. (**a**) Superposition of the band 3 membrane domain in $B_2P_1^{diagonal}$ complex and reported crystal structure (PDB: 4YZF)[16]. (**b**) Topology of the transmembrane helices of band 3. (**c**) Density of the DDM molecule at the interface of the core and gate domain. (**d**) Enlarged view of the substrate binding site in $B_2P_1^{diagonal}$ complex. Four water molecules were tentatively modelled into the cryo-EM density of band 3 near the substrate binding site. (**e**) Comparison of the substrate binding site in band 3 with that in bicarbonate transporter BicA (PDB: 6KI1)[25].

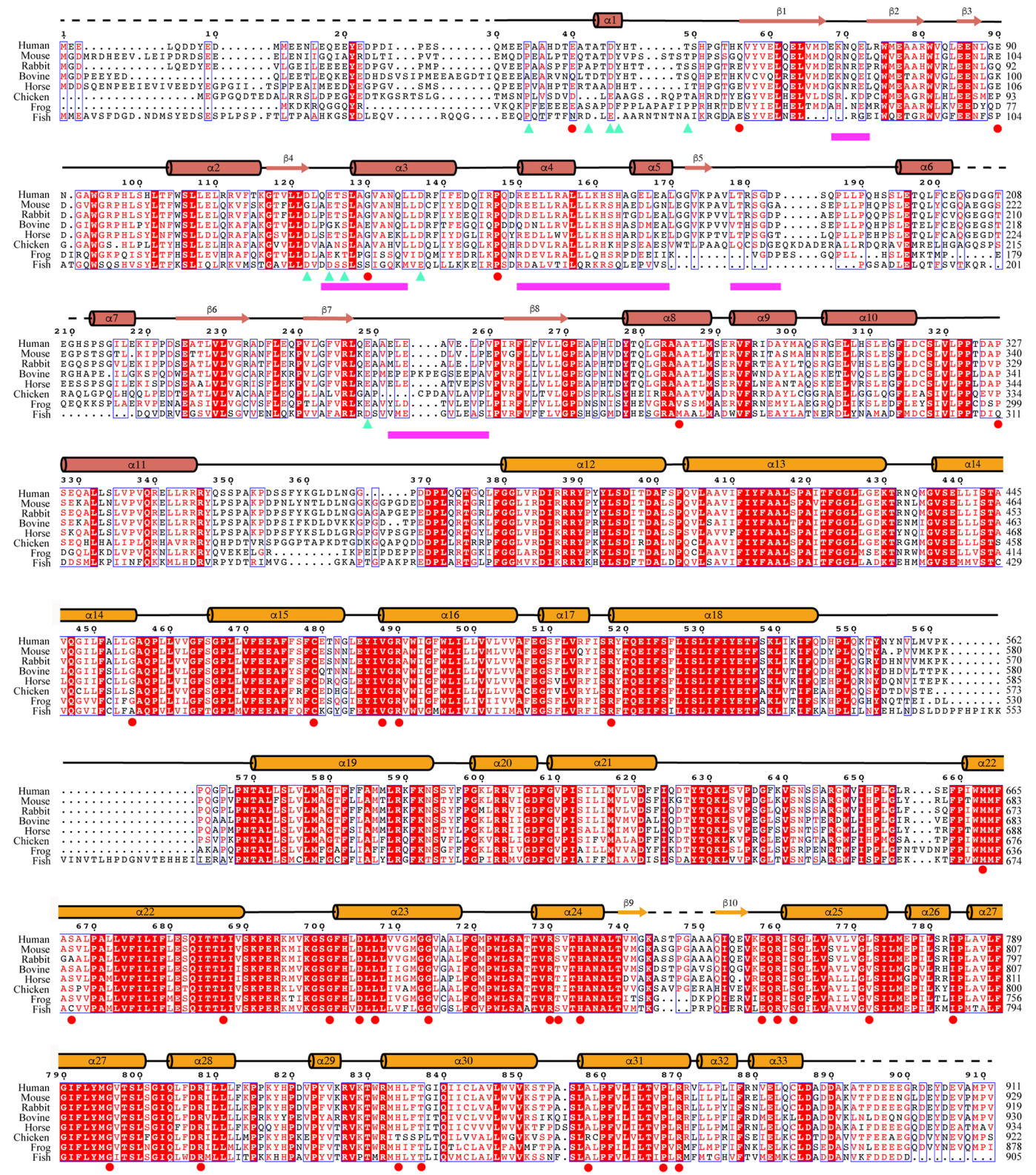

Extended Data Fig. 6 | Sequence alignment of band 3 from different species. Sequences of human band 3 (P02730), mouse band 3 (P04919), rabbit band 3 (G1SLY0), bovine band 3 (Q9XSW5), horse band 3 (Q2Z1P9), chicken band 3 (P15575), frog band 3 (F6XSL8) and fish band 3 (Q7ZZJ7). The sequence alignment is done using the Clustal Omega server[72]; the figure is generated by ESPript 3[73]. Cyan triangles represent the band 3 residues interacting with protein 4.2; magenta bars indicate the regions of band 3 interacting with ankyrin; reported disease mutations on human band 3 are labeled as red circles.

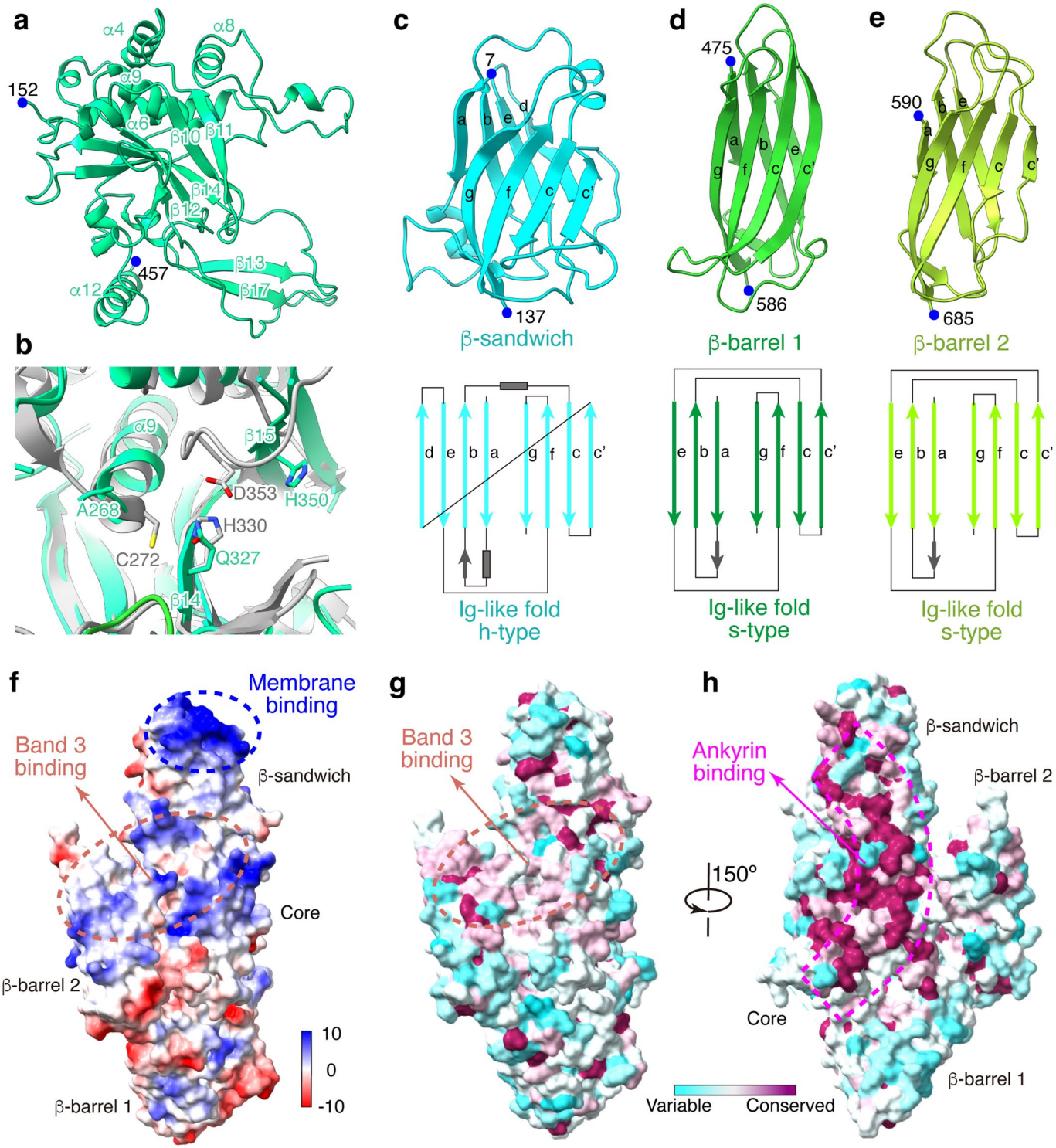

Extended Data Fig. 7 | Structure of protein 4.2. (**a**) Structure of the core domain shown in ribbon. Residue numbers of its N and C terminus are labeled. (**b**) Superposition of protein 4.2 with transglutaminase (gray, PDB: 1L9N)[31], showing the missing catalytic triad in protein 4.2. (**c-e**) Structures of the three Ig-like domains and illustrations of their secondary structure. (**f**) The electrostatic surface of protein 4.2, showing its membrane binding site (blue dashed circle) and band 3 binding interface (orange dashed circle). (**g-h**) Sequence conservation of protein 4.2 among mammals mapped to the structure. Orientation in (g) is the same as that in (f). Orange dashed circle shows the band 3 binding interface; magenta dashed box shows the ankyrin binding interface.

Extended Data Fig. 8 | Sequence alignment of protein 4.2 from different species. Sequences of human protein 4.2 (P16452), mouse protein 4.2 (P49222), rabbit protein (G1TDR3), bovine protein 4.2 (O46510), horse protein 4.2 (F6ZDW1), chicken protein 4.2 (E1BQZ4), frog protein 4.2 (XP_018090678.1) and human transglutaminase 3 (Q08188). The sequence alignment is done using the Clustal Omega server[72]; the figure is generated in ESPript 3[73]. Salmon triangles represent protein 4.2 residues interacting with band 3; magenta bars indicate the regions of protein 4.2 interacting with ankyrin; reported disease mutations on human protein 4.2 are labeled as red circles; black stars indicate the catalytic residues of human transglutaminase 3.

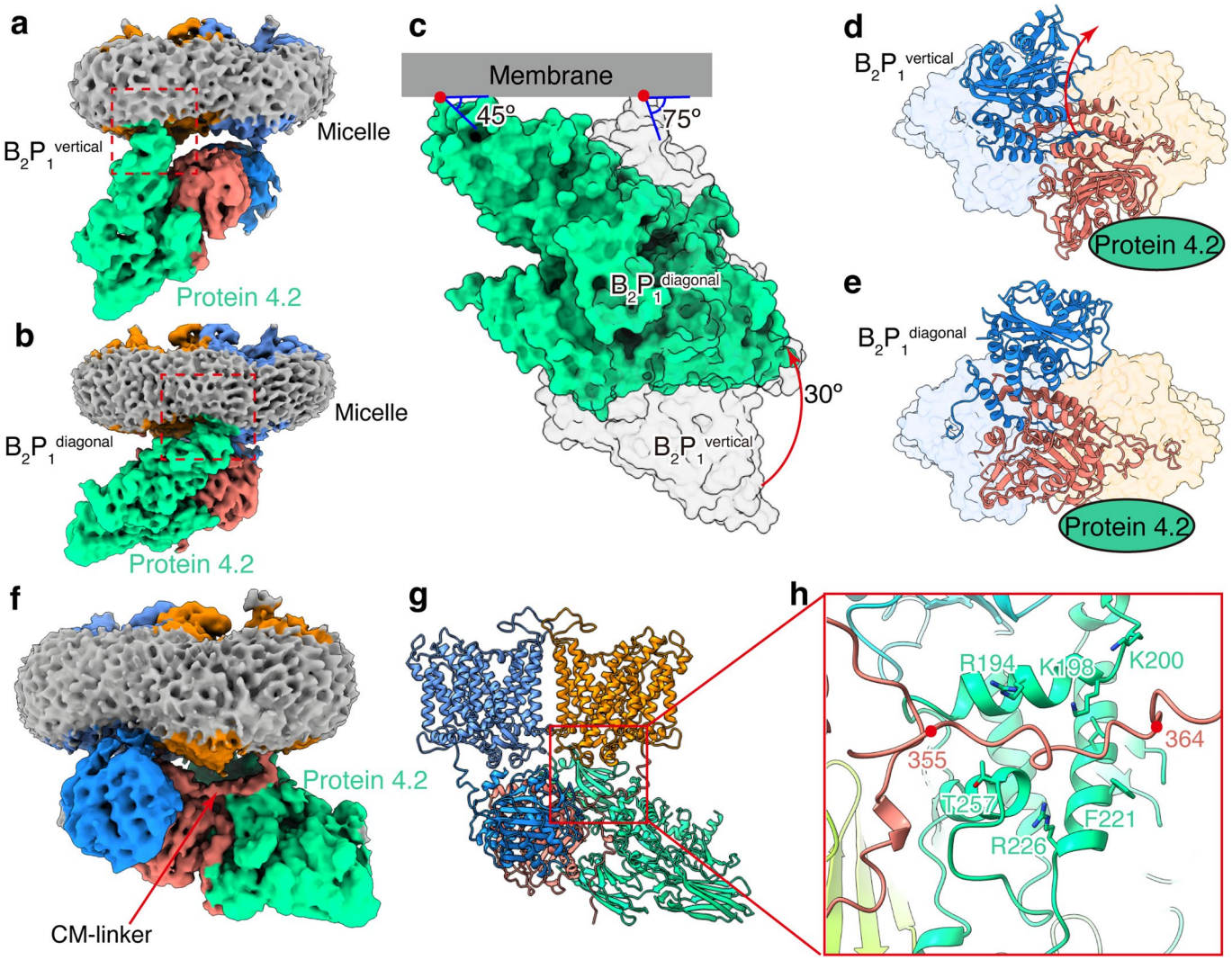

Extended Data Fig. 9 | Conformational changes of band 3 and protein 4.2 during the assembly process. (**a**, **b**) Density map of the $B_2P_1^{vertical}$ complex and $B_2P_1^{diagonal}$ complex. Red box indicates the anchorage site of protein 4.2 N-termini to the membrane. (**c**) Rotation of protein 4.2 (red arrow) from vertical (transparent grey surface) to diagonal conformation (green surface). The two complexes are superposed according to the membrane domains of band 3. The cytoplasmic domains of band 3 are omitted for clarity. Angles between the membrane (grey bar) and protein 4.2 are labeled. (**d-e**) Rotation of the cytoplasmic domain of band 3 (red arrow) from $B_2P_1^{vertical}$ to $B_2P_1^{diagonal}$ complex viewed from the cytoplasmic side. The membrane domain of band 3 is shown as transparent surface and cytoplasmic domain as ribbon. Protein 4.2 is indicated as a green oval for clarity. (**f**) Density map of the $B_2P_1^{diagonal}$ complex sharpened with B-factor of −50 Å^2 showing the interaction of the CM-linker with protein 4.2. (**g-h**) Ribbon representation of the CM-linker region. Residues of protein 4.2 interacting with the CM-linker are labeled.

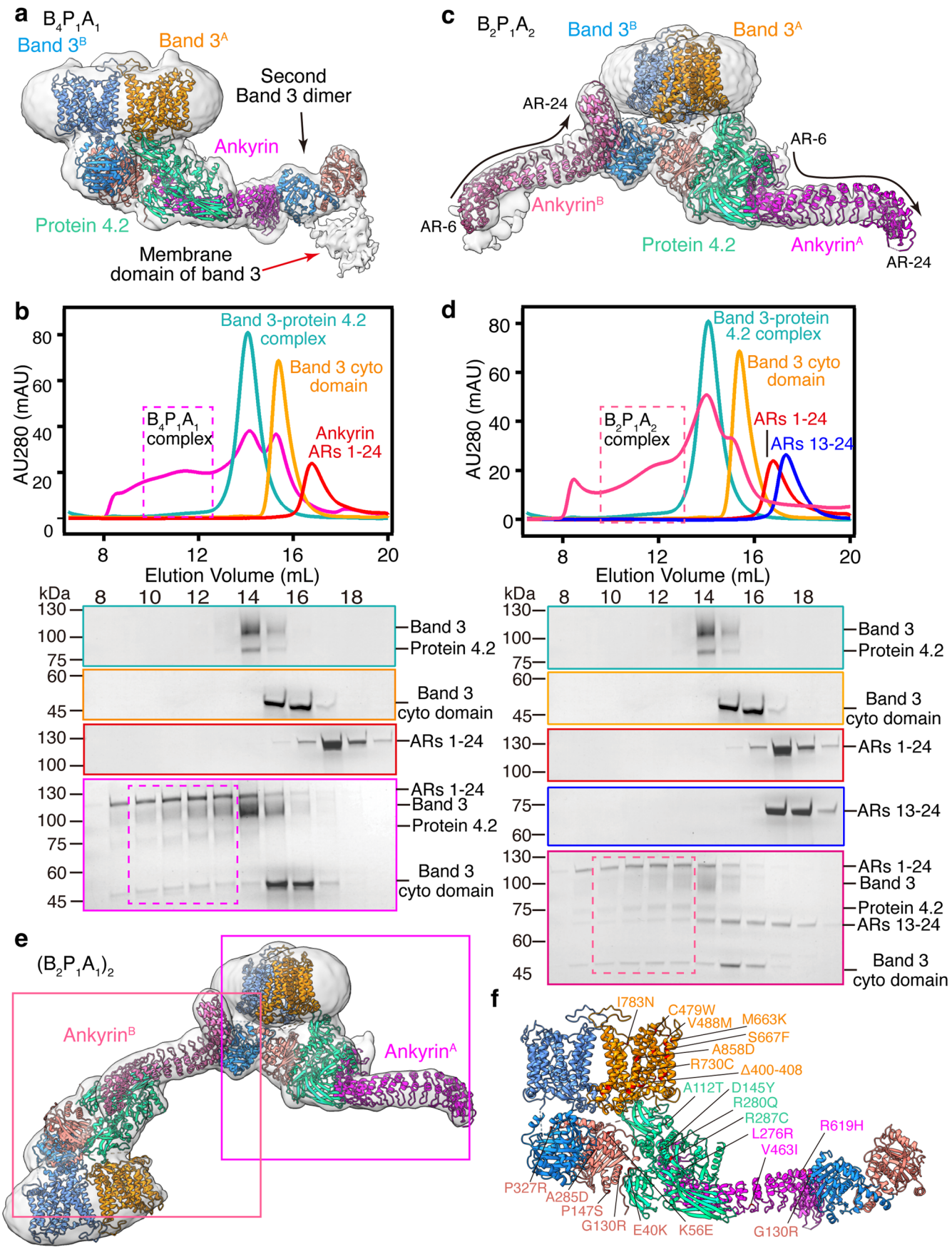

Extended Data Fig. 10 | See next page for caption.

Extended Data Fig. 10 | Analysis of the ankyrin-containing complexes. (**a**) Atomic model of $B_4P_1A_1$ complex in ribbon superposed with the density map at a low threshold. Red arrow indicates the density of the membrane domain of the second band 3 dimer. (**b**) Analytical gel filtration assay showing the assembly of $B_4P_1A_1$ complex in vitro. Dashed boxes show the position of $B_4P_1A_1$ complex. Experiments were repeated for two times with similar results. (**c**) Atomic model of $B_2P_1A_2$ complex in ribbon superposed with the density map at a low threshold. The density for the second band 3 dimer is indicated by arrow. (**d**) Analytical gel filtration assay showing the assembly of $B_2P_1A_2$ complex in vitro. Dashed boxes show the position of $B_2P_1A_2$ complex. The gel-filtration and SDS-PAGE results of protein 4.2 complex, band 3 cytoplasmic domain and ARs 1–24 are the same as that in (b). Second band 3 dimer may be incorporated into this complex, resulting in the $B_4P_1A_2$. Experiments were repeated for two times with similar results. (**e**) Atomic model of $(B_2P_1A_1)_2$ complex in ribbon superposed with the density map. Boxes show the position of individual $B_2P_1A_1$ complexes. (**f**) Reported disease mutations mapped on the structure of $B_4P_1A_1$ complex.

nature research

Corresponding author(s): Z.Hong Zhou

Last updated by author(s): Apr 3, 2022

Reporting Summary

Nature Research wishes to improve the reproducibility of the work that we publish. This form provides structure for consistency and transparency in reporting. For further information on Nature Research policies, see our Editorial Policies and the Editorial Policy Checklist.

Statistics

For all statistical analyses, confirm that the following items are present in the figure legend, table legend, main text, or Methods section.

n/a	Confirmed
☐	☒ The exact sample size (*n*) for each experimental group/condition, given as a discrete number and unit of measurement
☐	☒ A statement on whether measurements were taken from distinct samples or whether the same sample was measured repeatedly
☒	☐ The statistical test(s) used AND whether they are one- or two-sided *Only common tests should be described solely by name; describe more complex techniques in the Methods section.*
☒	☐ A description of all covariates tested
☒	☐ A description of any assumptions or corrections, such as tests of normality and adjustment for multiple comparisons
☒	☐ A full description of the statistical parameters including central tendency (e.g. means) or other basic estimates (e.g. regression coefficient) AND variation (e.g. standard deviation) or associated estimates of uncertainty (e.g. confidence intervals)
☒	☐ For null hypothesis testing, the test statistic (e.g. *F*, *t*, *r*) with confidence intervals, effect sizes, degrees of freedom and *P* value noted *Give P values as exact values whenever suitable.*
☒	☐ For Bayesian analysis, information on the choice of priors and Markov chain Monte Carlo settings
☒	☐ For hierarchical and complex designs, identification of the appropriate level for tests and full reporting of outcomes
☒	☐ Estimates of effect sizes (e.g. Cohen's *d*, Pearson's *r*), indicating how they were calculated

Our web collection on statistics for biologists contains articles on many of the points above.

Software and code

Policy information about availability of computer code

Data collection	SerialEM 3.9
Data analysis	Gautomatch_v0.53, Topaz v0.2.5, CTFFIND4, RELION3.1, cryoSPARC v3, UCSF Chimera 1.13 and ChimeraX 1.25, Resmap1.95, MotionCor2, Coot0.8.9, PHENIX 1.19, clustalW 2.1, ESPript 3.0

For manuscripts utilizing custom algorithms or software that are central to the research but not yet described in published literature, software must be made available to editors and reviewers. We strongly encourage code deposition in a community repository (e.g. GitHub). See the Nature Research guidelines for submitting code & software for further information.

Data

Policy information about availability of data

All manuscripts must include a data availability statement. This statement should provide the following information, where applicable:

- Accession codes, unique identifiers, or web links for publicly available datasets
- A list of figures that have associated raw data
- A description of any restrictions on data availability

Cryo-EM density maps have been deposited in the Electron Microscopy Data Bank under accession numbers EMD-26148 (band 3 dimer), EMD-26145 (loosely bound protein 4.2), EMD-26146 (vertical protein 4.2 complex), EMD-26147 (protein 4.2 dimer), EMD-26142 (diagonal protein 4.2 complex), EMD-26143 (membrane part of diagonal protein 4.2 complex), and EMD-26144 (cytoplasmic part of diagonal protein 4.2 complex), EMD-26149 (B2P1A1), EMD-26150 (focused refine of B2P1A1), EMD-26151 (B2P1A2), EMD-26152 (focused refine of B2P1A2), EMD-26153 (B4P1A1), EMD-26154 [(B2P1A1)2]. Model coordinates have been deposited in the Protein Data Bank under accession numbers 7TW2 (band 3 dimer), 7TW0 (vertical protein 4.2 complex), 7TW1 (protein 4.2 dimer), 7TVZ (diagonal protein 4.2 complex), 7TW3 (B2P1A1), 7TW5 (B2P1A2) and 7TW6 (B4P1A1).
Other structures used in this study were retrieved from the PDB with accession codes 4YZF for crystal structure of band 3 membrane domain, 1HYN for crystal

structure of band 3 cytoplasmic domain, 1N11 for ARs 13-24 of ankyrinR, 4RLV for ARs 1-24 of ankyrinB, 1L9N for transglutaminase 3 and 6KI1 for BicA.
All other data needed to evaluate the conclusions in the paper are present in the paper and/or the supplementary materials. Source data are provided with this paper.

Field-specific reporting

Please select the one below that is the best fit for your research. If you are not sure, read the appropriate sections before making your selection.

☒ Life sciences ☐ Behavioural & social sciences ☐ Ecological, evolutionary & environmental sciences

For a reference copy of the document with all sections, see nature.com/documents/nr-reporting-summary-flat.pdf

Life sciences study design

All studies must disclose on these points even when the disclosure is negative.

Sample size	A volume of 50 mL packed human red blood cells were used for each purification to generate enough protein for cryo-EM. Each dataset was collected in an independent Krios session, yielding particle numbers sufficient for following classification. A total of 9455, 20842 and 21187 micrographs were collected for band 3, band 3-protein 4.2 complex and ankyrin complex, respectively.
Data exclusions	For cryo-EM analysis, micrographs of low quality (<5%) were excluded by manual check. Particles that do not belong to the class of interest or have poor qualities based on well established cryoEM principle were excluded after rounds of 2D and 3D classification. This is standard in the single particle cryo-EM field. For functional studies, no data were excluded from any analysis.
Replication	Process of particle picking from the cryo-EM images was repeated with two different softwares with similar results. Refinements of the structures were repeated two times with similar 3D maps. All of the biochemical experiments were repeated two or more times with similar results.
Randomization	For cryo-EM, particles used in refinements were randomly split into two halves automatically in Relion and cross correlation coefficients (FSC curves) between two the half sets are calculated. Randomization is not applicable to the biochemical experiments in our study, because no grouping was needed.
Blinding	For cryo-EM, datasets were automatically split into two half in Relion. Blinding is not feasible for cryo-EM, because visual inspection is necessary to ascertain the data quality. For the biochemical experiments, blinding is not applicable as no grouping was needed for this study.

Reporting for specific materials, systems and methods

We require information from authors about some types of materials, experimental systems and methods used in many studies. Here, indicate whether each material, system or method listed is relevant to your study. If you are not sure if a list item applies to your research, read the appropriate section before selecting a response.

Materials & experimental systems

n/a	Involved in the study
☒	☐ Antibodies
☒	☐ Eukaryotic cell lines
☒	☐ Palaeontology and archaeology
☒	☐ Animals and other organisms
☒	☐ Human research participants
☒	☐ Clinical data
☒	☐ Dual use research of concern

Methods

n/a	Involved in the study
☒	☐ ChIP-seq
☒	☐ Flow cytometry
☒	☐ MRI-based neuroimaging